A CO isotopologue Line Atlas within the Whirlpool galaxy Survey (CLAWS)

Jakob S. den Brok, Frank Bigiel, Kazimierz Sliwa, Toshiki Saito, Antonio Usero, Eva Schinnerer, Adam K. Leroy, María J. Jiménez-Donaire, Erik Rosolowsky, Ashley T. Barnes, et al.

A&A 662, A89 (2022)
https://doi.org/10.1051/0004-6361/202142247

Astronomy & Astrophysics

A CO isotopologue Line Atlas within the Whirlpool galaxy Survey (CLAWS)

Jakob S. den Brok[1], Frank Bigiel[1], Kazimierz Sliwa[2], Toshiki Saito[2,3,4], Antonio Usero[5], Eva Schinnerer[2], Adam K. Leroy[6], María J. Jiménez-Donaire[5,7], Erik Rosolowsky[8], Ashley T. Barnes[1], Johannes Puschnig[1], Jérôme Pety[9,10], Andreas Schruba[11], Ivana Bešlić[1], Yixian Cao[11], Cosima Eibensteiner[1], Simon C. O. Glover[12], Ralf S. Klessen[12,13], J. M. Diederik Kruijssen[14], Sharon E. Meidt[15], Lukas Neumann[1], Neven Tomičić[16], Hsi-An Pan[2,17], Miguel Querejeta[5], Elizabeth Watkins[14], Thomas G. Williams[2], and David Wilner[18]

[1] Argelander-Institut für Astronomie, Universität Bonn, Auf dem Hügel 71, 53121 Bonn, Germany
e-mail: jdenbrok@astro.uni-bonn.de
[2] Max-Planck-Institut für Astronomie, Königstuhl 17, 69117 Heidelberg, Germany
[3] Department of Physics, General Studies, College of Engineering, Nihon University, 1 Nakagawara, Tokusada, Tamuramachi, Koriyama, Fukushima, 963-8642, Japan
[4] National Astronomical Observatory of Japan, 2-21-1 Osawa, Mitaka, Tokyo 181-8588, Japan
[5] Observatorio Astronómico Nacional (IGN), C/ Alfonso XII 3, 28014 Madrid, Spain
[6] Department of Astronomy, The Ohio State University, 4055 McPherson Laboratory, 140 West 18th Avenue, Columbus, OH 43210, USA
[7] Centro de Desarrollos Tecnológicos, Observatorio de Yebes (IGN), 19141 Yebes, Guadalajara, Spain
[8] 4-183 CCIS, University of Alberta, Edmonton, Alberta T6G 2E1, Canada
[9] Institut de Radioastronomie Millimétrique (IRAM), 300 Rue de la Piscine, 38406 Saint Martin d'Hères, France
[10] LERMA, Observatoire de Paris, PSL Research University, CNRS, Sorbonne Universités, 75014 Paris, France
[11] Max-Planck-Institut für extraterrestrische Physik, Giessenbachstraße 1, 85748 Garching, Germany
[12] Universität Heidelberg, Zentrum für Astronomie, Institut für Theoretische Astrophysik, Albert-Ueberle-Str 2, 69120 Heidelberg, Germany
[13] Universität Heidelberg, Interdisziplinäres Zentrum für Wissenschaftliches Rechnen, Im Neuenheimer Feld 205, 69120 Heidelberg, Germany
[14] Astronomisches Rechen-Institut, Zentrum für Astronomie der Universität Heidelberg, Mönchhofstraße 12–14, 69120 Heidelberg, Germany
[15] Sterrenkundig Observatorium, Universiteit Gent, Krijgslaan 281 S9, 9000 Gent, Belgium
[16] INAF-Osservatorio Astronomico di Padova, Vicolo Osservatorio 5, 35122 Padova, Italy
[17] Department of Physics, Tamkang University, No.151, Yingzhuan Rd., Tamsui Dist., New Taipei City 251301, Taiwan
[18] Center for Astrophysics | Harvard & Smithsonian, 60 Garden St., Cambridge, MA 02138, USA

Received 17 September 2021 / Accepted 22 December 2021

ABSTRACT

We present the CO isotopologue Line Atlas within the Whirpool galaxy Survey (CLAWS), which is based on an IRAM 30 m large programme that provides a benchmark study of numerous faint CO isotopologues in the millimetre-wavelength regime across the full disc of the nearby grand-design spiral galaxy M 51 (NGC 5194). The survey's core goal is to use the low-J CO isotopologue lines to constrain CO excitation and chemistry, and therefrom the local physical conditions of the gas. In this survey paper, we describe the CLAWS observing and data reduction strategies. We map the $J = 1 \rightarrow 0$ and $2 \rightarrow 1$ transitions of the CO isotopologues ^{12}CO, ^{13}CO, C^{18}O, and C^{17}O, as well as several supplementary lines within the 1 mm and 3 mm window (CN (1−0), CS (2−1), CH_3OH (2−1), N_2H^+ (1−0), and HC_3N (10−9)) at ∼1 kpc resolution. A total observation time of 149 h offers unprecedented sensitivity. We use these data to explore several CO isotopologue line ratios in detail, study their radial (and azimuthal) trends, and investigate whether changes in line ratios stem from changes in interstellar medium properties such as gas temperatures, densities, or chemical abundances. For example, we find negative radial trends for the ^{13}CO/^{12}CO, C^{18}O/^{12}CO, and C^{18}O/^{13}CO line ratios in their $J = 1 \rightarrow 0$ transitions. We also find variations with the local environment, such as higher ^{12}CO (2−1)/(1−0) or ^{13}CO/^{12}CO (1−0) line ratios in interarm regions compared to spiral arm regions. We propose that these aforementioned variations in CO line ratios are most likely due to a variation in the optical depth, though abundance variations due to selective nucleosynthesis on a galaxy-wide scale could also play a role. We also study the CO spectral line energy distribution (SLED) using archival JCMT ^{12}CO (3−2) data and find a variation in the SLED shape with local environmental parameters, suggesting changes in the optical depth, gas temperatures, or densities.

Key words. galaxies: ISM – ISM: molecules – radio lines: galaxies

1. Introduction

A key to our understanding of the interstellar medium (ISM) and its chemical evolution is the study of emission from carbon monoxide (CO), the second most abundant molecule after H_2, and its isotopologues. Such isotopologue studies allow us to examine the physical conditions within the gas, study the enrichment of the ISM, and open up the potential of deciphering the star formation history of a galaxy. Due to CO's permanent dipole moment and low mass, it has low-energy rotational transitions. Consequently, the emission from these rotational transitions is excited and can be observed at low temperatures (<10 K) – unlike for H_2, which is hardly excited and thus not observable under typical ISM conditions. While the low-J CO transitions of the main isotopologue, ^{12}CO, are known to be optically thick, a relation of their emission with the molecular gas mass has been found via the CO-to-H_2 conversion factor, α_{CO} (e.g. Solomon et al. 1987; Nakai & Kuno 1995; Leroy et al. 2011a; Sandstrom et al. 2013; or see review by Bolatto et al. 2013).

The ^{12}CO line brightness temperature ratios between different rotational transitions are generally of great interest. High-z observations typically observe higher-J ^{12}CO lines (Carilli & Walter 2013). By assuming line ratios, such studies can calculate an equivalent ^{12}CO (1–0) brightness temperature (e.g. Tacconi et al. 2008; Genzel et al. 2012; Cañameras et al. 2018) and then convert to physical parameters, such as the molecular gas mass, using α_{CO}. Such studies often adopt CO line ratios and a CO-to-H_2 conversion factor measured in the local universe (e.g. Tacconi et al. 2008; Schruba et al. 2012; Sandstrom et al. 2013, see also reviews by Solomon & Vanden Bout 2005; Carilli & Walter 2013). However, recent studies find variations in the line ratio within and among nearby spiral galaxies (den Brok et al. 2021; Yajima et al. 2021; Leroy et al. 2022), which have consequences for the down-conversion of high-J CO transitions and the conversion to ISM physical parameters. Such variations are also expected from simulations. Modelling individual giant molecular clouds, Peñaloza et al. (2018) found variations in the ^{12}CO line brightness temperature ratios of order 0.3 dex and attributed these changes to varying environmental conditions, including cloud mass and density, the interstellar radiation field (ISRF), and the cosmic ray ionisation rate (CRIR). Furthermore, the CO-to-H_2 conversion factor itself is subject to environmental variations (e.g. Young & Scoville 1982; Sandstrom et al. 2013; Accurso et al. 2017; see also simulations, e.g. Shetty et al. 2011a,b; Gong et al. 2018, 2020). The value for α_{CO} is empirically calibrated using many Milky Way clouds (Solomon et al. 1987), from CO, H I, and dust mass observations in external galaxies (Sandstrom et al. 2013), or using [C II] emission (Madden et al. 2020). When comparing α_{CO} to other galaxies, the metallicity, the presence of CO-dark gas, and temperature variations relative to the Milky Way should be taken into account. Thus, it is important to constrain variations in the CO line ratio and conversion factor and understand their dependences on the galactic environment and ISM conditions.

CO isotopologue transitions help us study the conditions of the ISM. Whereas the low ^{12}CO transitions usually remain optically thick, C^{18}O and C^{17}O lines stay optically thin over large parts of the galaxy. By contrast, the ^{13}CO emission can be optically thin or have a moderate optical depth, depending on its relative abundance (see the review by Heyer & Dame 2015). Comparing two optically thick lines provides insight into the physical conditions of the emitting gas, such as its temperature or density (Leroy et al. 2017; Jiménez-Donaire et al. 2019; den Brok et al. 2021). Contrasting optically thin to optically thick lines allows us to analyse the optical depth of the gas and investigate the gas column and volume densities of the molecular gas (Young & Scoville 1982; Pineda et al. 2008; Wilson et al. 2009). Finally, studying the ratio of two optically thin lines can be used to study abundance variations within the Milky Way (Langer & Penzias 1990; Milam et al. 2005) or across galaxy discs (Jiménez-Donaire et al. 2017b).

The study of CO isotopologues can also be used to investigate the chemical enrichment of the molecular gas. C and O isotopes – and consequently CO isotopologues – are a direct byproduct of stellar evolution via the CNO cycle. By studying their abundances, the physical processes that generate the various CO isotopologue species can be analysed. For instance, the ^{13}C isotope is primarily produced in low-mass stars (Wilson & Rood 1994), while ^{18}O is mainly replenished due to massive stars (Henkel et al. 1994). This makes the CO isotopologues a useful diagnostic tool for studying stellar populations (Sliwa et al. 2017; Sliwa & Downes 2017; Zhang et al. 2018; Brown & Wilson 2019). Previous studies of CO isotopologues and other C, N, and O isotope ratios have already been extensively carried out for the Milky Way (Langer & Penzias 1990; Wilson & Matteucci 1992; Wilson & Rood 1994; Henkel et al. 1994; Milam et al. 2005). The past decade has also seen an increase in the study of CO isotopologues in extragalactic sources (Martín et al. 2010; Henkel et al. 2014; Meier et al. 2015; Cao et al. 2017; Jiménez-Donaire et al. 2017a,b, 2019; den Brok et al. 2021; Yajima et al. 2021).

The low-J ^{12}CO transitions produce the brightest molecular lines (e.g. at 30 arcsec, we find brightness temperatures of around 60 K km s^{-1} in the centre of M 51) and consequently have been covered in numerous previous studies carried out with the Institut de Radioastronomie Millimétrique (IRAM) 30 m telescope, the IRAM Northern Extended Millimeter Array (NOEMA), the Atacama Large Millimeter/submillimeter Array (ALMA), and other millimetre-wavelength observatories (Hasegawa et al. 1997; Hasegawa 1997; Sakamoto et al. 1997; Leroy et al. 2009; Koda et al. 2011, 2020). CO isotopologue ratios are harder to observe since, due to their lower abundance, the emission is of order ∼10 and ∼50 times fainter for ^{13}CO and C^{18}O, respectively, compared to the ^{12}CO emission. Therefore, in the past these transitions were usually either studied in the Milky Way (Langer & Penzias 1990; Wilson & Rood 1994; Sawada et al. 2001; Yoda et al. 2010) or in strongly active star-forming galaxies, such as starburst galaxies or ultra-luminous infrared galaxies (ULIRGs; Meier & Turner 2004; Costagliola et al. 2011; Aladro et al. 2013; Sliwa et al. 2017; Brown & Wilson 2019). Only in recent years, thanks to the advancement of state-of-the-art receivers and large programmes, have we seen an increase in CO isotopologue line surveys of star-forming spiral galaxies.

The EMIR Multiline Probe of the ISM Regulating Galaxy Evolution (EMPIRE) survey targeted nine galaxies and covered the ^{13}CO and C^{18}O $J = 1 \rightarrow 0$ transitions (Jiménez-Donaire et al. 2019). It has been found, for example, that the ^{13}CO to C^{18}O line ratio is much lower in ULIRGs and star-bursting systems than compared to the Milky Way or nearby normal star-forming galaxies (Greve et al. 2009; Matsushita et al. 2009; Jiménez-Donaire et al. 2017b; Brown & Wilson 2019), consistent with recent or ongoing star formation as well as a top-heavy stellar initial mass function (Brown & Wilson 2019). Furthermore, Cormier et al. (2018) used the optically thin ^{13}CO (1–0) line from EMPIRE to derive a spatially resolved ^{13}CO-to-H_2 conversion factor for nearby galaxies.

With the CO Isotopologue Line Atlas within the Whirlpool galaxy Survey (CLAWS), we use the IRAM 30 m telescope to provide an in-depth analysis of low-J transitions of CO and

several isotopologues (^{13}CO, C^{18}O, and C^{17}O) over the entire star-forming and molecular disc (6.6 arcmin × 6.6 arcmin) of the grand-design spiral galaxy M 51 (NGC 5194). Due to its relative proximity (D = 8.6 Mpc; McQuinn et al. 2016) and high surface density, it is routinely observed from high-energy X-ray to radio wavelengths, thus providing a wealth of ancillary data. Previous wide field-of-view imaging observations have targeted different low-J ^{12}CO and ^{13}CO emission line transitions (e.g. Koda et al. 2011; Pety et al. 2013; Schinnerer et al. 2013 as part of PAWS; Jiménez-Donaire et al. 2019 as part of EMPIRE) and even C^{18}O was observed towards a few bright regions inside M 51 (see Schinnerer et al. 2010; Tan et al. 2011; Watanabe et al. 2014, 2016). We complement these studies and provide the currently most complete extragalactic CO isotopologue line atlas.

The main goal of this project is to use the large number of CO isotopologues to study the dependence of excitation on galactic environment and investigate isotopic abundance variations. In addition, we use the CO isotopologues to constrain the spatial variation in the CO-to-H_2 conversion factor.

This paper is organised as follows: In Sect. 2, we present and describe the IRAM 30 m observations as well as the ancillary data that are used in this paper. Section 3 explains how we convert observational measurements to physical quantities. The main results of the paper, which include the different CO line ratios as well as their spatial variations, are presented in Sect. 4. Finally, Sect. 5 discusses our findings and provides an outlook on future projects that can be conducted with the data from this project.

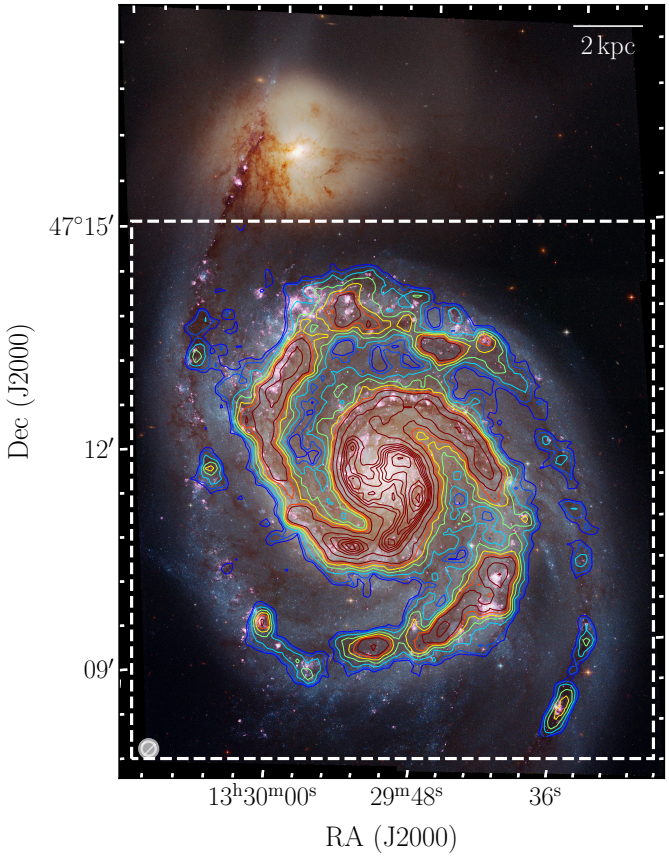

Fig. 1. Red, green, and blue (RGB) image of M 51 with ^{12}CO emission, a colour HST plate composed of B, V, and I filter images taken from Mutchler et al. (2005). Overlaid as contours are the IRAM 30 m ^{12}CO (2–1) integrated line brightness temperatures (at a resolution of 13 arcsec, indicated by the circle in the lower-left corner). The contours show signal-to-noise levels from 8 to 70, from blue to brown. The beam size of the ^{12}CO (2–1) observations is indicated at the bottom left of the figure. The dashed region shows the field-of-view of the IRAM 30 m observations.

2. Observations and data reduction

2.1. Target

M 51 (NGC 5194) is a prime target for the study of faint CO isotopologues in extragalactic systems. With a distance of $D \approx 8.6$ Mpc (McQuinn et al. 2016) – so an angular scale of 1 arcsec corresponds to physical scale of ∼40 pc – it is one of the brightest nearby grand-design spiral galaxies. It is a tidally interacting, active star-forming galaxy, with the molecular gas dominating the inner ∼5–6 kpc (Schuster et al. 2007; Leroy et al. 2008) Furthermore, the galaxy hosts an active galactic nucleus (Querejeta et al. 2016). Figure 1 shows the galaxy in the optical using a *Hubble* Space Telescope (HST) image. The ^{12}CO (2–1) emission observed as part of this programme is overlaid. The galaxy is close-to face on (i = 22°; Colombo et al. 2014) and the target's key parameters are listed in Table 1. M 51 is a template for active star-forming galaxies, where we can resolve discrete environments, know molecular cloud properties (e.g. from PAWS; Colombo et al. 2014) and have a wealth of ancillary data and observations from all wavelength regimes. The ancillary data used in this study are provided and described in the following sections.

2.2. Observations

As part of an IRAM 30 m large programme (#055-17), the EMIR receiver was used to map emission lines in the 1 mm (220 GHz) and 3 mm (100 GHz) windows in dual polarisation from the entire disc of M 51 for a total of 149 h (109.2 h on-source time) between 2017 and 2019. The receiver has an instantaneous bandwidth of 15.6 GHz per polarisation. The observations were split into two parts by implementing E90 LO/LI + UI/UO (Setup 1) as well as E230 LO/LI + UI/UO (Setup 2). The first setup covers the 3 mm range and was carried out under good atmospheric conditions (1.8 mm of precipitable water vapour (pwv) and mean $T_{\rm sys}$ = 111 K [$T_{\rm a}^{\star}$]). The total on-source time accumulated to 65.9 h. The second setup observes $J = 2 \rightarrow 1$ lines in the 1 mm regime. For this setup, good winter conditions were required (1.7 mm pwv and $T_{\rm sys}$ = 217 K [antenna temperature $T_{\rm a}^{\star}$] mean) and the final total on-source time amounted to 43.3 h. The fast Fourier transform spectrometers with 195 kHz spectral resolution (FTS200) were used for both setups to provide a spectral resolution of ∼0.5 km s^{-1} for the E090 and ∼0.2 km s^{-1} for the E230 band. Table 2 lists the lines covered.

A field of 6.6 arcmin × 6.6 arcmin (around 44 arcmin^2) was mapped in the on-the-fly–position switching (OTF-PSW) mode and included two emission-free reference positions nearby. The mapping approach is similar to the one used in the EMPIRE survey (see Jiménez-Donaire et al. 2019). For each spectral setup, a scan of 8 arcsec s^{-1} is performed using multiple paths that are each offset by 8 arcsec from each other. For each execution of the mapping script, the scanned box is shifted by $\sqrt{2} \times (0, 2, 4, 6)$ along the diagonal. So in the end, M 51 is covered with a much finer, 2 arcsec instead of 8 arcsec, grid. The read-out dump time is 0.5 s, the final spacing between data points is 4 arcsec. The focus of the telescope was determined using observations of bright quasars or planets at the beginning of each observation

Table 1. M 51 source description.

Property	Value
Name	NGC 5194 (M 51)
RA (J2000) [(a)]	$13^{h}29^{m}52\overset{s}{.}7$
Dec (J2000) [(a)]	47°11′43″
i [(b)]	22°
PA [(c)]	172°
r_{25} [(d)]	3.9′
D [(e)]	8.6 Mpc
$V_{\rm hel}$ [(f)]	456.2 km s^{-1}
Metallicity [(g)] [12 + log(O/H)]	8.55
Morphology [(h)]	SAbc
$\langle\Sigma_{\rm SFR}\rangle$ [(i)]	20×10^{-3} $M_\odot$ yr^{-1} kpc^{-2}
$\log_{10}(M_\star/M_\odot)$ [(j)]	10.5

Notes. [(a)]Coordinates of the centre of the galaxy adopted from the NASA Extragalactic Database (NED) from Shetty et al. (2007). [(b)]Inclination of the galaxy with respect to the plane of the sky from Colombo et al. (2014). [(c)]Position angle of the galaxy. [(d)]25th magnitude isophote radius of the B-band taken from the Extragalactic Distance Database (EDD; Tully et al. 2009). [(e)]Distance to the galaxy from McQuinn et al. (2016). [(f)]Heliocentric systemic velocity from Walter et al. (2008). [(g)]Metallicity averaged across the full galaxy from Moustakas et al. (2010). [(h)]Morphological type as given in Leroy et al. (2013). Adopted from Dale et al. (2009). [(i)]The average SFR surface density within $0.75r_{25}$. [(j)]Integrated stellar mass derived from 3.6 µm emission.

session, which had typical lengths of 2–3 h. In the case of longer sessions, the focus was corrected every 3 h, and in addition after sunset and sunrise. Every 1–1.5 h, the pointing of the telescope was adjusted using either a nearby quasar or planet. In order to properly perform the antenna temperature ($T_{\rm a}^\star$) calibration, a chopper-wheel calibration was done repeatedly every 10–15 minutes using a hot- and a cold-load absorber and sky measurements. Finally, line calibrators (IRC+10216, W3OH, and W51D) were routinely observed to monitor systematic error in amplitude and the flux calibration.

2.3. Data reduction

The data reduction was performed automatically using the scripts and pipeline used for the EMPIRE survey (see description in Jiménez-Donaire et al. 2019). Basic calibration was done using `MRTCAL`[1]. The first step consists of converting the spectrum to the antenna temperature scale. For this, each science scan is combined with the last previous calibration scan. Next, we subtract from the calibrated spectrum the OFF measurement. These steps constitute the most basic calibration. The target lines are then extracted using the Continuum and Line Analysis Single-dish Software (`CLASS`[2]). A zeroth-order baseline is subtracted, omitting the range of 50–300 km s^{-1} around the centre of the line in the fit. The individual spectra are then re-gridded to have a 4 km s^{-1} channel width across the full bandpass. The spectra are saved as FITS files for further processing.

In order to monitor the stability of the flux calibration, the spectra of line-calibrator sources (e.g. IRC+10216) were further obtained. From these we find a maximum day-to-day variation in amplitude of ∼7.5% over all observations. The 1σ variation is ∼2.4% only.

Subsequent data reduction is performed using a custom `IDL` routine based on the HERA CO-Line Extragalactic Survey (HERACLES) data reduction pipeline (Leroy et al. 2009). This routine removes pathological data such as bad scans or spectra. Platforming correction at the edges of the FTS units is also corrected for in the EMPIRE pipeline. The baseline fitting is performed again excluding a generous line window using the ^{12}CO (1–0) line emission from PAWS as a prior: Around the mean ^{12}CO (1–0) velocity, a window is placed, the full width of which ranges between 50 and 300 km s^{-1} depending on the width of the line for each pixel. Two further windows of the same width are defined adjacent to the central window and a second-order polynomial fit of the baseline is performed in these windows. The resulting baseline is subtracted from the entire spectrum.

After these steps, we check for further pathological spectra. These are rejected by sorting the remaining spectra by their rms, which is calculated from the line-free windows after the baseline subtraction, and the highest 10% are rejected. Upon careful inspection by eye, additional spectra were discarded if they showed platforming or other potential issues.

The antenna temperature scale ($T_{\rm a}^\star$) is converted to main beam temperature ($T_{\rm mb}$) using a cubic interpolation of the forward ($F_{\rm eff}$) and beam ($B_{\rm eff}$) efficiencies from the IRAM documentation[3] as a function of the observing frequency. In particular, the conversion is performed using the following equation:

$$T_{\rm mb} = \frac{F_{\rm eff}}{B_{\rm eff}} T_{\rm a}^\star. \quad (1)$$

The $F_{\rm eff}/B_{\rm eff}$ ratio adopted for our observing programme was 1.2 for Setup 1 (3 mm regime) and 1.6 for Setup 2 (1 mm regime). In this study, we exclusively use the main beam temperature $T_{\rm mb}$.

The final data cube is generated by gridding the spectra onto a 2 arcsec spaced Cartesian grid. Consequently, the final resolution is coarser than the IRAM 30 m native resolution due to the gridding kernel by a factor of 1.2.

We do not correct for the contribution from the IRAM 30 m error beam to the observed main beam temperature. We discuss this effect in Appendix A. In short, emission can enter our detection via the telescope's error beam, thus increasing the observed flux. Regions with faint emission in the galaxy are most likely affected by this. The exact shape of the IRAM 30 m error beam is difficult to determine and it fluctuates depending on the telescope's elevation. Consequently, we can only estimate the impact. We see that in the 3 mm regime, the contribution leads to an additional 10% increase in flux in faint regions. In the 1 mm regime, the impact is larger with a contribution of up to 30 to 40% in certain regions. For a more detailed discussion of the estimation of error beam contributions, we refer the reader to Appendix A.

2.4. Ancillary data

2.4.1. PAWS ^{12}CO (1–0) emission line data

The PdBI Arcsecond Whirlpool Survey (PAWS)[4] covers the ^{12}CO (1–0) line emission at 1 arcsec (≈40 pc) resolution across the full disc of M 51 (Schinnerer et al. 2013). The survey

[1] https://www.iram-institute.org/medias/uploads/mrtcal-check.pdf
[2] https://www.iram.fr/IRAMFR/GILDAS/doc/html/class-html/class.html
[3] The online IRAM documentation can be found at http://www.iram.es/IRAMES/mainWiki/Iram30mEfficiencies
[4] Data can be downloaded from https://www2.mpia-hd.mpg.de/PAWS/PAWS/Data.html

Table 2. Summary of the lines covered in CLAWS, the key observational parameters, and key characteristics of the extracted data products.

Setup	Band	Line	$\nu_{\rm rest}$ (GHz)	Beam size ($''$) (1)	Beam size (kpc) (1)	On-source time (h) (2)	$\langle T_{\rm sys}\rangle$ (K) (3)	$\langle$pwv$\rangle$ (mm) (4)
1	E0 (3 mm)	CN (1−0)	113.250	26.1	1.1	44.5	111	1.8
		$C^{17}O$ (1−0)	112.359	26.3	1.1			
		^{13}CO (1−0)	110.201	26.8	1.1			
		$C^{18}O$ (1−0)	109.782	26.9	1.1			
		CS (2−1)	97.981	30.2	1.3			
		CH_3OH (2−1)	96.700	30.6	1.3			
		N_2H^+ (1−0)	93.173	31.7	1.3			
		HC_3N (10−9)	90.897	32.5	1.4			
2	E2 (1.3 mm)	^{12}CO (2−1)	230.538	12.8	0.53	20.9	217	1.7
		^{13}CO (2−1)	220.399	13.4	0.56			
		$C^{18}O$ (2−1)	219.560	13.5	0.56			

Notes. (1) Beam size of the final data cube after reduction. (2) Total on-source time (spectral time) excluding additional telescope overheads. (3) Average system temperature. (4) Average precipitable water vapour (pwv) during observations.

combines observations from IRAM's Plateau de Bure Interferometer (PdBI) and the IRAM 30 m single dish telescope. We only use the IRAM 30 m observations for this work, as we do not require high spatial resolution. The data reduction is described in Pety et al. (2013). Observations were carried out in 2010 and the data have a native spatial resolution of 23 arcsec (≈1.0 kpc) with an 1σ noise level of 16 mK at 5 km s^{-1} spectral resolution.

2.4.2. NGLS ^{12}CO (3–2) emission line data

As part of the *James Clerk Maxwell* Telescope (JCMT) Nearby Galaxy Legacy Survey (NGLS; Wilson et al. 2012), the ^{12}CO (3−2) emission across the full disc of M 51 was mapped (Vlahakis et al. 2013). Observations with an angular resolution of 14.5 arcsec (≈600 pc) were carried out with the 16 pixel array receiver HARP-B at the JCMT between 2007 and 2009.

2.4.3. THINGS 21 cm H I emission line data

The H I data[5] from the H I Nearby Galaxy Survey (THINGS; Walter et al. 2008) is used to map the atomic gas content across the full disc of M 51. The H I emission is of particular interest, as it is very extended, making it a good prior for masking emission regions outside the central region of the galaxy. The survey employed the Very Large Array (VLA). The natural weighted data used in this study have an angular resolution of ∼10 arcsec (≈400 pc) and a spectral resolution of ∼5 km s^{-1}.

2.4.4. High-density EMPIRE emission line data

The EMPIRE survey (Jiménez-Donaire et al. 2019) covered the emission of a number of high-density emission lines in the 3 mm regime, such as HNC (1−0), HCN (1−0) or HCO^+ (1−0), across the entire star-forming disc of a sample of nine nearby spiral galaxies. The survey uses observations[6] carried out with the EMIR receiver at the IRAM 30 m single dish telescope. The science goal of the survey was to take deep and extended intensity maps of high critical density lines tracing the dense gas content in the galaxy. While the $J = 1 \rightarrow 0$ transition of ^{13}CO is also covered in the survey, we only consider the high-density lines HCN (1−0) HNC (1−0), and HCO^+ (1−0) in our study and rely on our own ^{13}CO (1−0) observation (since our observations are deeper).

2.4.5. VNGS infrared data

Infrared broadband data in the range of 3.6 to 500 µm are taken from the Very Nearby Galaxy Survey (VNGS; Parkin et al. 2013). These observations were carried out using the Multiband Imaging Photometer for *Spitzer* (MIPS) instrument on board the *Spitzer* Space Telescope, as well as Photodetector Array Camera & Spectrometer (PACS) and the Spectral and Photometric Imaging Receiver (SPIRE) instruments on board the *Herschel* Space Observatory. The infrared bands are used to estimate the total infrared (TIR) emission and star formation rate (SFR; see Sect. 3.3).

2.5. Final data products

Due to the large wavelength range covered, we have a variety of spatial resolutions for our observations, ranging from 12.8 arcsec/500 pc for ^{12}CO (2−1) to 32.5 arcsec/1.3 kpc for HC_3N (10−9). To properly match and compare observations of different emission lines, we convolve to the same working resolution and re-project all data to a common grid. In this study we use three different working resolutions: (i) 15 arcsec/600 pc, analysis involving ^{12}CO (2−1) and (3-2); (ii) 27 arcsec/1.1 kpc, analysis involving all CO isotopologues; and (iii) 34 arcsec/1.4 kpc, analysis involving all molecular lines.

Table 3 lists the working resolutions used for every line in our sample. The data are finally resampled onto a hexagonal grid with a grid size of half the beam size (see Fig. 2, note that lines observed as part of other programmes than CLAWS are marked with an asterisk). Re-gridding onto a hexagonal grid is commonly done in the literature (see e.g. Bigiel et al. 2011; Leroy et al. 2013; Sandstrom et al. 2013; Cormier et al. 2018). One advantage over a Cartesian grid is the

[5] Available at https://www2.mpia-hd.mpg.de/THINGS/Data.html

[6] Details on the survey and the data can be found at https://empiresurvey.webstarts.com/index.html

Table 3. Lines covered as part of CLAWS with measurements re-gridded onto the same hexagonal grid and convolved to a common working resolution: 15, 27, or 34 arcsec.

					35″/1.4 kpc aperture [(a)]			60″/2.4 kpc aperture [(a)]		
Band	Line	Resolution (″)	$T_{\rm peak}$ (mK)	⟨rms⟩ (mK)	$W_{\rm line}$ (K km s^{-1})	$S/N_{\rm line}$	$W_{\rm line}/W_{^{12}{\rm CO}\,(2-1)}$	$W_{\rm line}$ (K km s^{-1})	$S/N_{\rm line}$	$W_{\rm line}/W_{^{12}{\rm CO}\,(2-1)}$
		(1)	(2)	(3)	(4)	(5)	(6)	(7)	(8)	(9)
3 mm	CN (1−0)	34	32	4.4	1.7	66	0.05	1.1	50	0.04
	$C^{17}O$ (1−0)	27	26	5.8	0.23	10	0.006	0.1	11	0.007
		34	20	4.2						
	^{13}CO (1−0)	27	142	4.9	5.5	250	0.15	4.2	280	0.15
		34	116	3.6						
	$C^{18}O$ (1−0)	27	40	4.7	1.2	52	0.033	0.9	47	0.030
		34	33	3.4						
	CS (2−1)	34	15	3.0	0.6	35	0.016	0.4	36	0.014
	CH_3OH (2−1)	34	13	2.8	0.2	9	0.004	0.1	7	0.004
	N_2H^+ (1−0)	34	14	3.0	0.3	19	0.007	0.2	11	0.006
	HC_3N (10−9)	34	16	3.7	0.2	10	0.006	0.2	15	0.007
1 mm	^{12}CO (2−1)	15	1420	20	37	710	1.0	29	750	1.0
		27	850	10.6						
		34	730	8.8						
	^{13}CO (2−1)	15	185	17.6	3.3	67	0.09	2.3	73	0.08
		27	103	9.2						
		34	88	7.7						
	$C^{18}O$ (2−1)	15	88	18.3	0.9	21	0.03	0.6	21	0.02
		27	51	9.4						
		34	41	7.8						

Notes. [(a)]Emission of the central region convolved to the given aperture size. (1) Working resolutions used for each molecular line. (2) Maximum peak temperature observed across the full map of M 51 for a given emission line at a given working resolution. (3) Average channel rms sensitivity at 4 km s^{-1} channel width. (4, 7) Velocity-integrated brightness temperature within the central aperture. (5, 8) S/N within the central aperture. (6, 9) line ratio of a given line with respect to the velocity-integrated ^{12}CO (2−1) brightness temperature.

equidistance to the neighbouring pixels allowing for a more uniform sampling. Furthermore, since the beam shape is circular, given that the neighbourhood for a hexagonal grid also grows with some circularity, beam effects are captured. Using a half beam-sized hexagonal grid, we have an oversampling factor[7] of $N_{\rm s} = 4.p6$. The spectra for all lines, sampled in the aforementioned way, are combined into a final data structure for further analysis.

We determine the velocity-integrated brightness temperature by integrating masked spectra of individual sight lines. For the innermost part of the galaxy up to a galactocentric radius of a CO scale length of $0.23r_{25}$ (Leroy et al. 2008; Lisenfeld et al. 2011; Puschnig et al. 2020)[8], we use the ^{12}CO (2−1) emission line as a prior for masking. For larger radii, where the CO emission becomes faint, we use the 21 cm H I emission line. By only integrating over the masked velocity region, we can improve the S/N significantly, which is essential to capture also the fainter line emission. The mask is produced by first flagging high S/N voxels in the ^{12}CO (2−1) or H I data, respectively ($S/N > 4$ for both). An additional, lower S/N mask (S/N>2) is produced using the same lines and voxels from the high mask, which are then expanded into the low mask. The velocity-integrated brightness temperature and its uncertainty, for both we are adopting units of K km s^{-1} throughout this work, are given by:

$$W_{\rm line} = \sum^{n_{\rm chan}} T_{\rm mb}(v) \cdot \Delta v_{\rm chan} \quad (2)$$

$$\sigma_W = \sqrt{n_{\rm chan}} \cdot \sigma_{\rm rms} \cdot \Delta v_{\rm chan}, \quad (3)$$

where $n_{\rm chan}$ is the masked number of channels along a line of sight, $T_{\rm mb}$ is the surface brightness temperature of a given channel in K, $\sigma_{\rm rms}$ is the position-dependent 1σ root-mean-squared (rms) value of the noise in K, and $\Delta v_{\rm chan}$ is the channel width in km s^{-1}. We calculated $\sigma_{\rm rms}$ over the signal-free part of the spectrum using the `astropy` function `mad_std`. It calculates the median absolute deviation and scales the result by a factor 1.4826 to yield a standard deviation (the factor follows from the assumption that noise follows a Gaussian distribution).

Table 3 provides a summary of the lines observed by CLAWS, as well as information about the data such as the average rms or the S/N of the line detection over a certain aperture. Figure 3 shows spectra of all these lines stacked over the central 1.5 kpc region. All the data of this project are made publicly available on the IRAM Large Programme website[9].

[7] We define the oversampling factor by the ratio of the beam area over the pixel size: $N_{\rm s} = (1.13 \times \theta^2_{\rm FWHM})/A^{\rm hex}_{\rm pix}$. Since we sample the data hexagonally, the pixels have a hexagonal shape with the long diagonal being equal to half the beam full width at half maximum.

[8] At a radial distance of $0.23r_{25}$, it has been found that the CO surface brightness has dropped, on average, by a factor of $1/e$ (see for more details Puschnig et al. 2020).

[9] https://www.iram-institute.org/EN/content-page-434-7-158-240-434-0.html

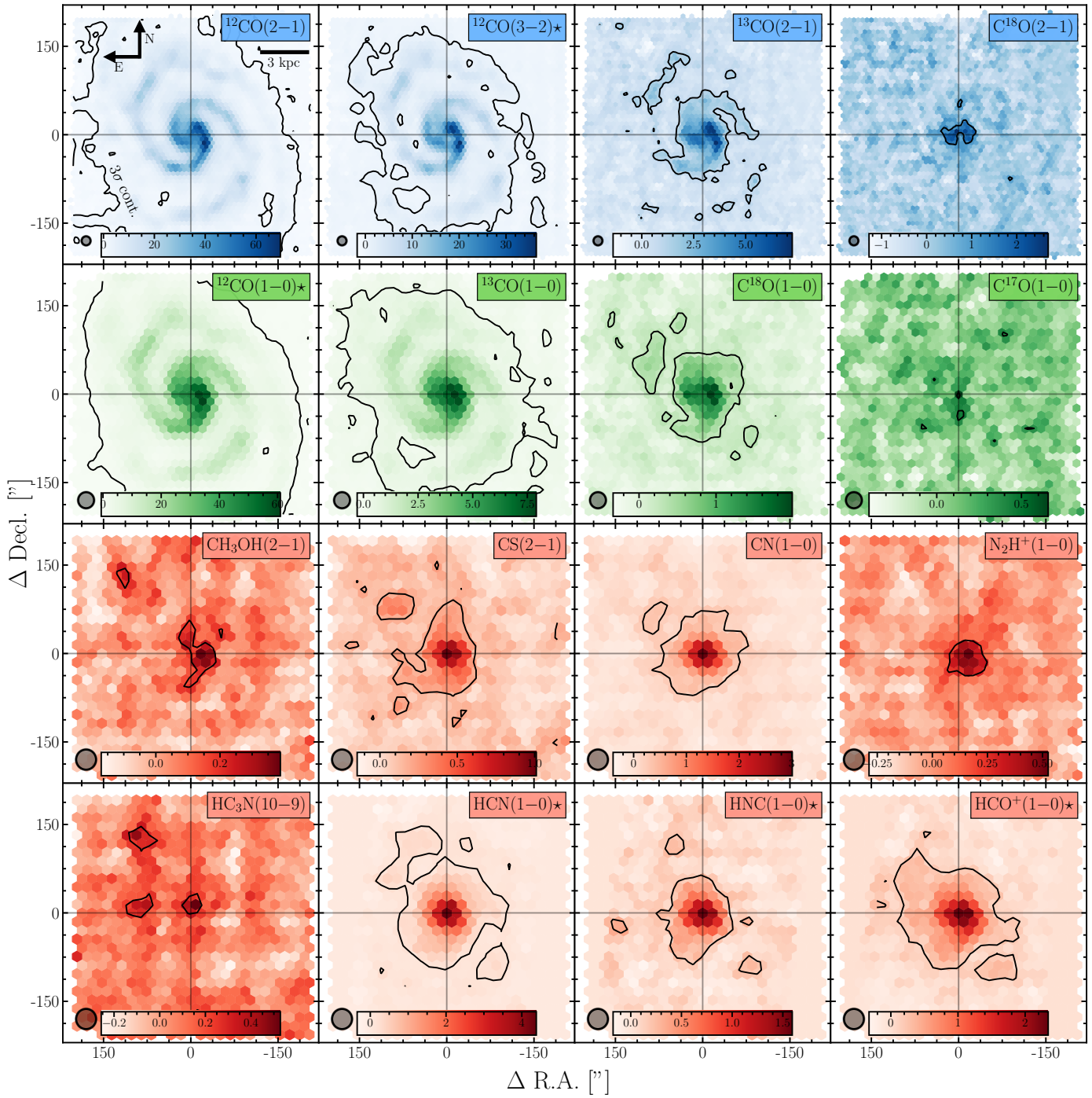

Fig. 2. Maps of the velocity-integrated brightness temperature for all lines used in this study. The maps are convolved to certain common beam sizes and re-gridded onto a common hexagonal grid, which allows a more uniform sampling. The top row (blue) is at 15 arcsec resolution, the second row (green) at 27 arcsec, and the remaining two rows (red) are convolved to 34 arcsec (corresponding to 0.62, 1.1, and 1.4 kpc, respectively). The grid spacing is chosen to be half the beam size. The velocity-integrated brightness temperature is in units of K km s^{-1}. The coordinates are relative to the centre coordinates given in Table 1. The black line indicates the $S/N = 3$ contour. Lines observed by other programmes are indicated by an asterisk after the line name in each panel. ^{12}CO (1−0) is part of the PAWS survey (Schinnerer et al. 2013; Pety et al. 2013), ^{12}CO (3−2) is taken from the NGLS survey (Wilson et al. 2012), and HCN (1−0), HNC (1−0), and HCO$^+$ (1−0) are emission lines obtained by the EMPIRE survey (Jiménez-Donaire et al. 2019).

3. Physical parameter estimation

We largely follow the methodology described in Cormier et al. (2018) investigating ^{13}CO line emission in EMPIRE galaxies and the EMPIRE survey paper by Jiménez-Donaire et al. (2019). The line ratios are measured as a function of galactocentric radius, ^{12}CO (2−1) brightness temperature and TIR surface brightness. For completeness, we also include the derived physical quantities of the molecular gas mass surface density ($\Sigma_{\rm mol}$) and the SFR surface density ($\Sigma_{\rm SFR}$), which we corrected for the inclination of M 51 by applying the factor cos(i). We note, however, that the conversion from observed to physical quantity is subject to

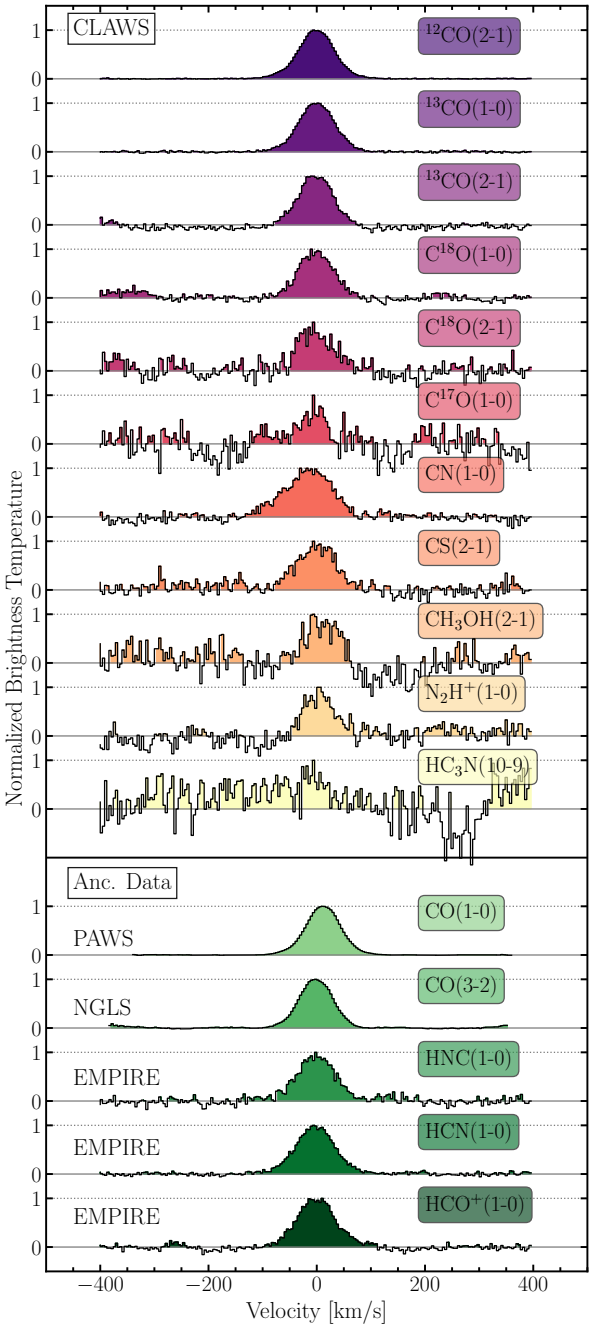

Fig. 3. Spectra of emission lines covered by this programme stacked over the central 1.5 kpc region at 34″. The emission lines are normalised to the maximum in the spectrum. The five bottom spectra are taken from different observing programmes (see Sect. 2.4), while the spectra above come from this project. For the absolute intensities, we refer the reader to Table 3. We note that we employ a hexagonal, half-beam-sized sampling. The angular resolution of 34″ corresponds to a physical scale of around 1.4 kpc. Therefore, the stacked spectra over the central 1.5 kpc region are thus the combination of the spectra of the seven most central sampling points.

uncertainties (see e.g. Kennicutt & Evans 2012; Bolatto et al. 2013; Usero et al. 2015).

3.1. Line ratio

Line ratios are determined by taking the velocity-integrated brightness temperatures of two lines, in units of K km s^{-1}, and dividing them. This is done for every line of sight as well as for the stacked spectra (see Sect. 3.2). The uncertainty of a line ratio, $R = W_1/W_2$, is given by the propagated uncertainty of the two lines:

$$\sigma_R = \frac{W_1}{W_2}\sqrt{\left(\frac{\sigma_{W_1}}{W_1}\right)^2 + \left(\frac{\sigma_{W_2}}{W_2}\right)^2}. \tag{4}$$

We generally express the average line ratio, $\langle R \rangle$, in terms of the ^{12}CO (2−1) brightness temperature weighted median, which is equivalent to the weighted 50th percentile. Given the ordered set of line ratios R for N lines of sight, with associated (but not necessarily ordered) ^{12}CO (2−1) surface brightness of $W_{^{12}\mathrm{CO\,(2-1)}}$

$$\left\{\left(R^i, W^i_{^{12}\mathrm{CO\,(2-1)}}\right)\right\}_{i=1,\ldots,N} \quad \text{for} \quad R^{i+1}_{^{12}\mathrm{CO\,(2-1)}} \geq R^i_{^{12}\mathrm{CO\,(2-1)}}, \tag{5}$$

and defining the relative weight as

$$w_i = \frac{W^i_{^{12}\mathrm{CO\,(2-1)}}}{\sum_{i=1}^{N} W^i_{^{12}\mathrm{CO\,(2-1)}}}, \tag{6}$$

the weighted pth percentile is given by the element R^k:

$$Q^w_p(R) = R^k \quad \text{satisfying} \quad \sum_{i=1}^{k} w_i \leq p \text{ and } \sum_{i=k+1}^{N} w_i \leq 1 - p. \tag{7}$$

Following this definition, we defined the ^{12}CO (2−1) brightness temperature weighted median line ratio as

$$\langle R \rangle \equiv Q^w_{0.5}(R). \tag{8}$$

The uncertainty of the weighted average line ratio is given by the 16th and 84th weighted percentile range throughout the study.

We constructed the line ratios such that the generally brighter line is in the denominator and the, overall, fainter line is in the numerator. As a consequence, we generally find upper limits, while lower limits are very rare.

Furthermore, because we compare lines with different S/N, we try to estimate the region in the plot in which we cannot obtain any measurements. Such a censored region occurs, for example, if we investigate the line ratio of a fainter line to a brighter line. Given that we have the same observed sensitivity, lower line ratios will be 'censored' since we reach the detection threshold for the faint line, while larger line ratios can still be observed, as they could originate from points with brighter emission of the faint line. To estimate the censored region, we first bin the line ratios by a certain quantity (such as the galactocentric radius). Since we constructed the line ratios such that the (generally) fainter line is in the numerator, we estimate the censored 1σ (or 3σ) region by dividing the average rms (or three times this value) of the faint line per bin by the average brightness temperature of the brighter line. We notice that because the rms and the line brightness vary across the survey field, we do find also points within the censored region.

3.2. Spectral stacking

In order to improve the S/N, which is especially crucial for fainter emission lines, we apply a spectral stacking technique. A detailed description of the stacking technique is given in several previous studies (e.g. Cormier et al. 2018; Jiménez-Donaire et al. 2019; den Brok et al. 2021). In short, the spectral axis of each

cube is re-gridded such that the emission line of each sight line is centred at $v = 0\,\mathrm{km\,s^{-1}}$. At $r_{\rm gal} < 0.23 r_{25}$, ^{12}CO (2−1) is used as the reference line, while at $r_{\rm gal} \geq 0.23 r_{25}$, H I is used. We note that for sight lines with both H I and CO detection, we find good agreement between their centroid velocities. With this approach, we can stack the lines of sight by a predefined quantity (for example galactocentric radius or ^{12}CO brightness temperature) and obtain an average spectrum for every bin. We stacked all lines of sight, irrespective of their individual S/N. We note that by stacking we disregard the intrinsic scatter of the data. Line ratios are then calculated from the velocity-integrated brightness temperatures of two (separately) stacked emission lines. Again, for an illustration of stacked spectra, we refer the reader to Fig. 3, which shows stacked spectra of the observed emission lines for the central region ($r_{\rm gal} < 1.5\,\mathrm{kpc}$). With the exception of HC_3N (10−9), all emission lines are significantly detected at $S/N > 3$ within the centre.

3.3. Total infrared surface brightness

The TIR surface density can be used as a proxy of the local surface density of star formation. Following Galametz et al. (2013), the TIR surface brightness ($\Sigma_{\rm TIR}$) takes the subsequent form:

$$\Sigma_{\rm TIR} = \sum_i c_i \Sigma_i, \tag{9}$$

with Σ_i being the surface brightness of the *Herschel* bands and c_i coefficients depending on the number of infrared bands available (see Table 3 in Galametz et al. 2013 for numerical values of the coefficients). We take the same approach as previous studies (e.g. Usero et al. 2015; Jiménez-Donaire et al. 2017b; Cormier et al. 2018) by combining the *Herschel* 70, 100, and 160 µm bands to estimate the TIR surface brightness. The maps are first convolved to the common beam size of 30 arcsec using the kernels described in Aniano et al. (2011). In their study, Galametz et al. (2013) indicated that the combination of the *Herschel* 70, 100, and 160 µm bands has a coefficient of determination[10] of $R^2 = 0.97$, meaning that the calibration we use accounts for 97% of the total variation in the TIR surface brightness.

From the TIR surface brightness we can estimate the SFR surface density. We adopted the calibration given by Murphy et al. (2011):

$$\left(\frac{\Sigma_{\rm SFR}}{M_\odot\,\mathrm{yr^{-1}\,kpc^{-2}}}\right) = 1.48\times10^{-10}\left(\frac{\Sigma_{\rm TIR}}{L_\odot\,\mathrm{kpc^{-2}}}\right). \tag{10}$$

It can been seen that, compared to the far-ultraviolet (FUV) plus 24 µm SFR prescription, a scatter of 40% is expected based on comparisons between the two prescriptions using resolved measurements in M33 (Williams et al. 2018).

3.4. Molecular gas mass surface density

The molecular gas mass surface density can be estimated from the ^{12}CO (1−0) line emission or from ^{12}CO (2−1) data using the well calibrated CO line ratio, $R_{21}^{^{12}\rm CO}$ (which we measure in this project). The conversion from CO emission to gas mass surface density relies on the CO-to-H_2 conversion coefficient, $\alpha_{\rm CO}$, as

$$\begin{aligned}\left(\frac{\Sigma_{\rm mol}}{M_\odot\,\mathrm{pc^{-2}}}\right) &= \alpha_{\rm CO} W_{\rm CO\,(1-0)}\cos(i)\\ &= \alpha_{\rm CO}\frac{W_{\rm CO\,(2-1)}}{R_{21}^{^{12}\rm CO}}\cos(i).\end{aligned} \tag{11}$$

For the $\alpha_{\rm CO}$ parameter usually the Milky Way value of is chosen $\alpha_{\rm CO} = 4.4\ M_\odot\,\mathrm{pc^{-2}}\ (\mathrm{K\,km\,s^{-1}})^{-1}$ (which includes a factor 1.36 for helium) in the case of massive galaxies with solar metallicity (Bolatto et al. 2013). Galaxy-to-galaxy as well as galaxy-internal variations in the conversion factor have been observed, but studies of nearby main sequence galaxies find largely values of similar order to those in the Milky Way (Sandstrom et al. 2013; Cormier et al. 2018). We note, however, that these $\alpha_{\rm CO}$ calibrations may not account for CO-dark gas, which could significantly impact the conversion factor in certain regions (see e.g. Gratier et al. 2017; Chevance et al. 2020; Madden et al. 2020).

4. Results

4.1. CLAWS line emission

Figure 2 shows the velocity-integrated brightness temperature maps of the lines covered as part of this programme (see coloured panels), all convolved to a common working beam size of 15, 27, or 34 arcsec (corresponding to 0.62, 1.1, or 1.4 kpc, respectively). The ^{12}CO and ^{13}CO emission, and to some extent the $C^{18}O$ (1−0) emission are clearly extended and M 51's spiral structure is visible by eye. The fainter $C^{18}O$ (2−1) and $C^{17}O$ (1−0) isotopologue lines are only detected in the centre of the galaxy. Besides the CO isotopologues, the other molecular lines are all confined to the centre of the galaxy. This is most likely just attributed to a lack of S/N at larger radii and not necessarily evidence of the molecule being truly more centrally concentrated. We explore radial trends for the CO lines in the following sections. Regarding emission from the centre, we see that for the CO isotopologues, the emission peaks are slightly offset towards the western spiral arm of the galaxy. By contrast, for the dense gas tracers, the emission seems to peak directly in the centre. Radial stacking improves the significant detections of faint emission lines. Among the non-CO lines part of CLAWS, with the reached sensitivity of $1\sigma_{\rm rms}$~4 mK at 4 km s^{-1}, only the CN (1−0) and CS (2−1) emission show radial extension out to $r_{\rm gal} \sim 3$ kpc (see Fig. 2).

4.2. CO emission line ratios

Line ratios can give insight into the physical conditions of the gas from which the emission originates. For example, under local thermodynamic equilibrium (LTE) conditions, contrasting optically thin and thick lines allows us to draw conclusions about the optical depth, while comparing two optically thin lines allows for investigating molecular abundances.

In Fig. 4, we inspect spatial variations for a selection of four CO line ratios with a large number of significantly detected sight lines. The figure shows the line ratio maps for ^{12}CO (2−1)/(1−0), ^{12}CO (3−2)/(2−1), ^{13}CO/^{12}CO (1−0), and $C^{18}O$/^{12}CO (1−0) (only for sight lines detected above 5σ in both lines). On the one hand, the ^{12}CO lines are generally optically thick so their line ratios relate to gas density or temperature as well as optical depth. (For ^{12}CO (2−1)/(1−0), we find also a non-negligible fraction of values with line ratios >1 at the edges

[10] The coefficient of determination is equal to the square of Pearson's linear correlation coefficient.

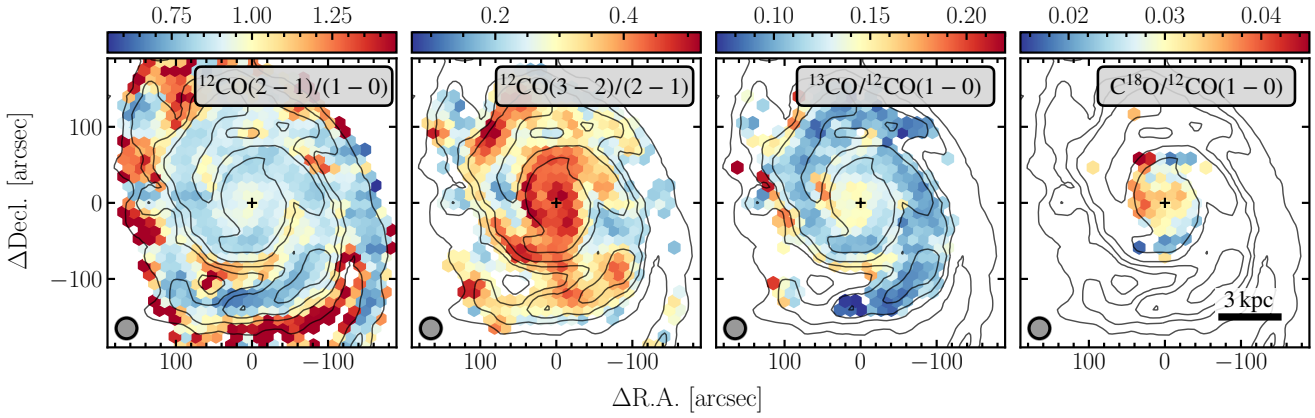

Fig. 4. CO line ratio maps for four selected ratios. All panels show the data convolved to 27 arcsec (indicated by circles in the lower-left corners). Only lines of sight with $S/N > 5$ in both lines are shown. Contours in each panel show the ^{12}CO (2−1) emission at 2, 4, 6, 10, and 20 K km s^{-1}. A local enhancement of the line ratio in the centre of the galaxy (indicated by a plus sign) is clearly visible for ^{12}CO (3−2)/(2−1) *(second to left panel)* and to some extent also for ^{12}CO (2−1)/(1−0) *(left and second to right panels)*. The C^{18}O (2−1)/^{12}CO (1−0) *(right panel)* is only significantly detected in the centre of the galaxy.

Table 4. CO line ratios and galactic environment.

Line ratio	Global	Central 45″	Arm	Interarm
^{12}CO (2−1)/(1−0)	$0.89^{+0.11}_{-0.07}$	$0.91^{+0.03}_{-0.05}$	$0.85^{+0.09}_{-0.05}$	$0.93^{+0.11}_{-0.07}$
^{12}CO (3−2)/(2−1)	$0.37^{+0.09}_{-0.11}$	$0.42^{+0.04}_{-0.05}$	$0.31^{+0.06}_{-0.07}$	$0.26^{+0.07}_{-0.05}$
^{13}CO/^{12}CO (1−0)	$0.12^{+0.02}_{-0.02}$	$0.14^{+0.01}_{-0.02}$	$0.11^{+0.01}_{-0.02}$	$0.12^{+0.03}_{-0.02}$

Notes. The CO (2−1) brightness temperature weighted mean line ratios and weighted 16th and 84th percentiles are given for different galactic environments.

of the map. Such line ratios would require optically thin ^{12}CO gas. However, at the edge of the map, S/N effects can drive up the ratio as well.) On the other hand, ^{13}CO and C^{18}O are generally optically thinner, thus making it possible to investigate their optical depths. Just qualitatively assessing the spatial variations and trends, we see that there is a tendency of higher line ratios in the centre. Furthermore, ^{12}CO (2−1)/(1−0) shows clear arm–interarm differences. Along spiral arms, the ratio is lower (∼0.85) than in interarm regions (∼0.93; see Table 4). We note that this finding is opposite to the results from Koda et al. (2012), who found a larger line ratio in spiral arm regions (see Sects. 4.4 and 5.1 for more details). For the C^{18}O/^{12}CO (1−0) line ratio, we only detect significant sight lines in the centre. With the help of stacking, we can get significant detections also at larger galactocentric radii ($r_{\rm gal} < 6$ kpc), showing a moderate negative radial trend.

In Fig. 5, we investigate the distributions of all CO isotopologue line ratios. These line ratios span a range of around 2 dex. ^{12}CO (2−1)/(1−0) shows the highest line ratio with CO (2−1) brightness temperature weighted mean of $0.89^{+0.11}_{-0.07}$. The lowest line ratio is given by C^{18}O/^{12}CO (1−0) with weighted mean of $0.031^{+0.004}_{-0.006}$. The individual ratios show a 95% inclusion region of ∼0.5 to 1 dex. The inset panel shows the effect of increasing the S/N cut of the ^{12}CO(2–1)/(1–0) line ratio. We do not find a significant difference in terms of the mean line ratio with increasing S/N cut.

We also studied the line ratios binned by galactocentric radius, CO (2−1) brightness temperature and TIR surface brightness. We ordered the CO line ratios into three categories: (i) fixed CO isotopologue, different transition (Fig. 6); (ii) different CO isotopologue, fixed $J = 1 \rightarrow 0$ (Fig. 7); and different CO isotopologue, fixed $J = 2 \rightarrow 1$ (Fig. 8).

We used the highest working resolution possible for each line ratio. For ratios involving the C^{17}O (1−0) line, we use the lowest resolution of 34 arcsec to maximise sensitivity. We define all line ratios such that the fainter line is in the numerator and the brighter one in the denominator. As a consequence, line ratios in faint regions may (frequently) appear as upper limits, while lower limits are very rare.

In Figs. 6, 7, and 8, we present our measurements in two ways: (i) we plot the line ratios of individual sight lines as a function of galactocentric radius, CO (2−1) brightness temperature and TIR surface brightness, and (ii) we stack the emission line spectra within bins of galactocentric radius, CO (2−1) brightness temperature and TIR surface brightness, and plot the line ratio of these stacked spectra. We note that the sample of sight lines usually differs between case (i) where only those sight lines are shown for which both lines have $S/N > 5$ and case (ii) where all sight lines are included in the stacked spectra while (again) only those line ratios are shown for which both stacked lines have $S/N > 5$. We stress that extrapolating these trends based on the stacked points to the individual lines of sight should be done with caution, as by stacking, we discard the intrinsic scatter of the data. This difference in sample implies that frequently the line ratio from stacked spectra does not coincide with the 'middle' of the line ratio distribution for individual sight lines (which provide a biased view as long as non-detections are neglected). The censored regions are described in Sect. 3.1 and show regions in the ratio space that we cannot sample due to the limited sensitivity. In these censored regions line ratios from stacked

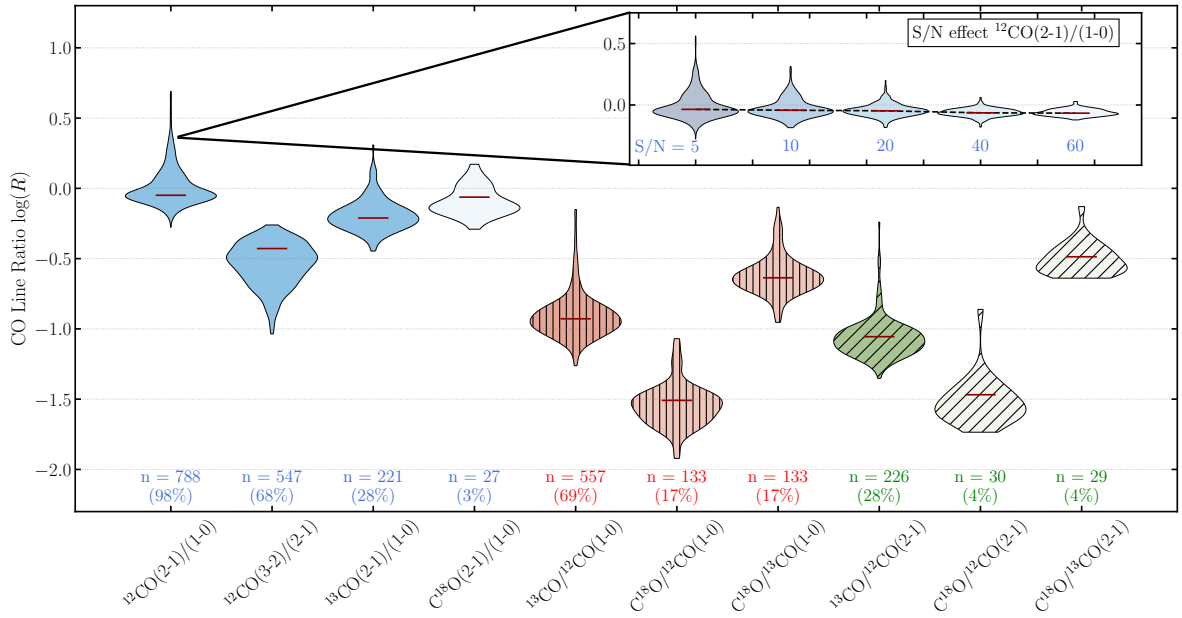

Fig. 5. Distribution of CO line ratios at 27 arcsec. The violin plots are colour-coded: blue indicates ratios of fixed CO isotopologue but different transitions, while red (vertically hatched) and green (diagonally hatched) show ratios of different CO isotopologue but fixed transition. The number of significant data points ($S/N > 5$) for each line ratio is indicated with n and the saturation of the colour of each violin. The percentage in terms of total detection is also indicated (with respect to $S/N > 5$ detected ^{12}CO(1–0) data points). In the inset panel, we show the effect of increasing the S/N cut from $S/N = 5$–60 for the ^{12}CO(2–1)/(1–0) line ratio. We do not find a significant difference in terms of the mean line ratio with increasing S/N.

spectra should be considered as these provide a robust and unbiased measurement (since they include non-detected sight lines).

Table 5 lists the Kendall's τ rank correlation coefficient as well as its significance, the p-value, of various line ratios based on the stacked data points that have $S/N > 5$. We employed the Kendall's τ rank correlation coefficient to measure a monotonic increasing, non-linear relationship in our data. It is more robust to error and discrepancies in the data (Croux & Dehon 2010) than the widely used Spearman's rank correlation coefficient. We also do not use the Spearman's rank correlation coefficient, since it is more sensitive to our choice of binning of the stacked data points. For the calculation of the coefficients for the CO line ratios as a function of galactocentric radius, we only included stacked points at $r_{\rm gal} \leq 5$ kpc. Since ^{12}CO (1–0) has the highest sensitivity and this transition appears in the denominator of our line ratios, this leads to line ratio for individual sight lines to turn upwards at larger radii or at fainter CO (2–1) brightness temperatures. To avoid this, we only include stacks with $W_{\rm CO\,(2-1)} > 2\,{\rm K\,km\,s^{-1}}$ for computation of Kendall's τ for the CO line ratios as a function of CO (2–1) brightness temperature. We do not compute the correlation coefficients for CO line ratios with only two or less significantly stacked points.

4.2.1. Fixed CO isotopologue – different transitions

Figure 6 shows fixed CO isotopologue line ratios for the three lowest rotational transitions. Such line ratios can give insight into the excitation state of the ISM. Looking at the line ratios as a function of galactocentric radius, we see that especially the stacked measurements of ^{12}CO (3–2)/(2–1) and ^{13}CO (2–1)/(1–0) show negative trends with both having a Kendall's rank correlation coefficient of $\tau = -0.80$ ($p = 0.083$). Within the central region ($r_{\rm gal} < 1$ kpc), the line ratios are enhanced by 37% for ^{12}CO (3–2)/(2–1) and 45% for ^{13}CO (2–1)/(1–0) as compared to the average stacked line ratio for $r_{\rm gal} < 5$ kpc. An increase in the line ratio within the centre of the galaxy is also qualitatively visible in Fig. 4 (see second to left panel for ^{12}CO (3–2)/(2–1)). Conversely, the ^{12}CO (2–1)/(1–0) line ratio does not show a significant trend with galactocentric radius, it shows only a slight enhancement of 5% in the centre over the average within 5 kpc. For C^{18}O (2–1)/(1–0), we do not have enough significantly detected stacked spectra to investigate a trend with radius.

For the line ratios as a function of the ^{12}CO (2–1) brightness temperature, only ^{12}CO (3–2)/(2–1) shows a significant positive trend with Kendall's $\tau = 1.00$ ($p = 0.003$). However, we note that especially for lower CO brightness temperatures, the effect of correlated axes might enhance such a trend. Both the ^{12}CO (2–1)/(1–0) and ^{13}CO (2–1)/(1–0) line ratios do not show any clear trend with CO brightness temperature. However, for ^{13}CO (2–1)/(1–0), we find a positive trend in the range $W_{\rm CO\,(2-1)} > 2\,{\rm K\,km\,s^{-1}}$.

Finally, considering the line ratios as a function of the TIR surface brightness, we again find positive trends for ^{12}CO (3–2)/(2–1) with $\tau = 1.0$ ($p = 0.083$). While, for ^{12}CO (2–1)/(1–0), we find a flat trend with respect to $\Sigma_{\rm TIR}$. Due to the faintness of the C^{18}O (2–1) line, we do not have enough significant points for the C^{18}O (2–1)/(1–0) line ratio to determine if any trend exists.

Of particular conspicuousness is the fact that the stacked ^{12}CO (3–2)/(2–1) line ratio shows opposite trends in every column (i.e. with galactocentric radius, CO brightness temperature and TIR surface brightness) compared to the ^{12}CO (2–1)/(1–0) line ratio. This is opposite to the notion that both ratios show a similar behaviour, but could be coupled to the fact that ^{12}CO (3–2) is more constrained to the denser regions of the molecular ISM.

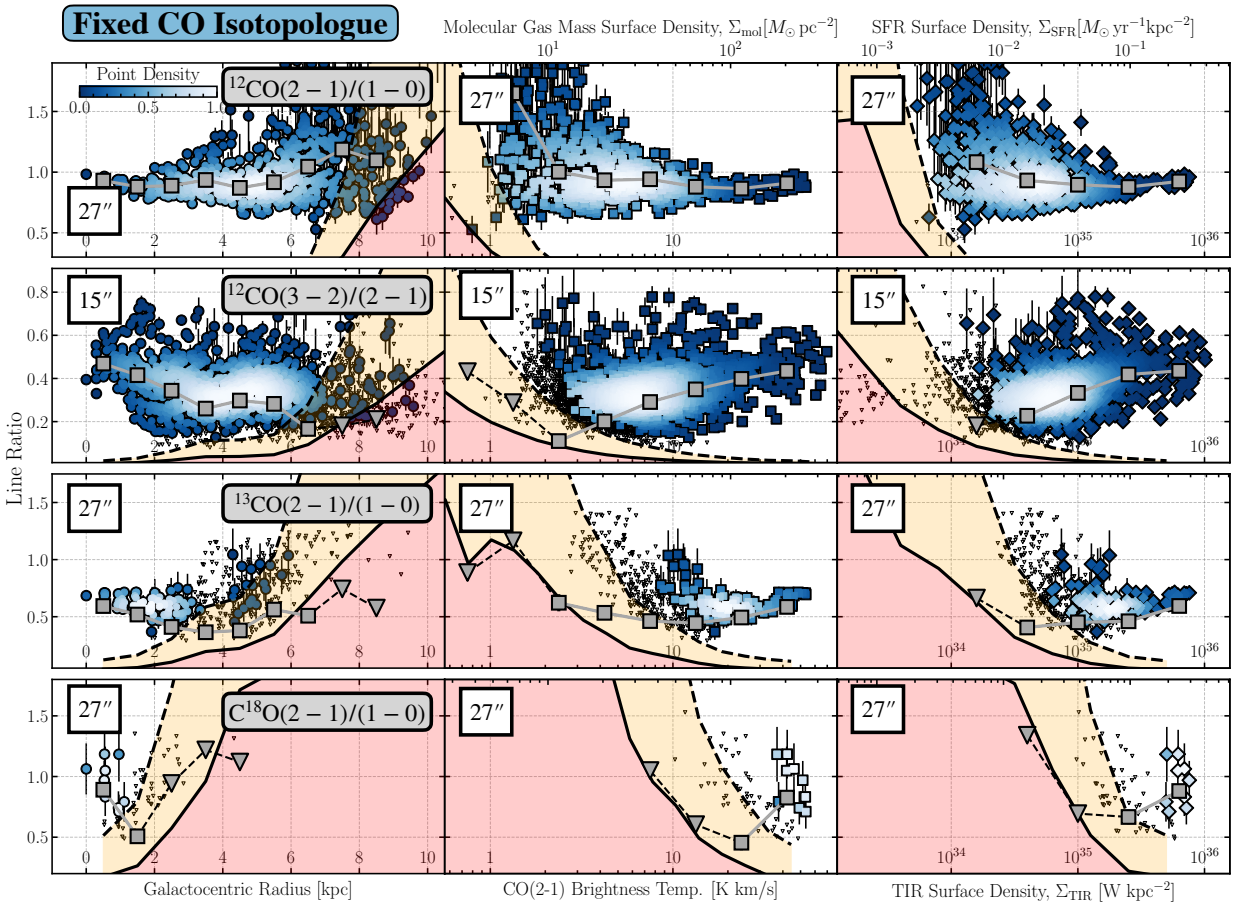

Fig. 6. CO line ratios as a function of galactocentric radius, CO (2−1) brightness temperature, and TIR surface brightness. Each row shows the line ratio for individual lines of sight for fixed CO isotopologues but different transitions. Each column shows the CO line ratio as a function of galactocentric radius, CO (2−1) brightness temperature, and TIR surface brightness. The coloured data points show the individual lines of sight with a $S/N > 5$, and the small black downward triangles indicate 3σ upper limits. To illustrate the point density in the figure, we colour-code the points using a 2D KDE. Values are normalised to the peak density and range from most dense (1; white) to least dense (0; blue) The shaded area in each panel shows the 1σ (red) and 3σ (orange) censored regions for the individual lines of sight. They are an estimate of where we expect to no longer be able to detect line ratios (due to the low S/N of one of the lines). Marked in grey are the line ratios derived from the stacked spectra (downward triangles again mark upper limits). Error bars for significant points are indicated (for the stacked data points, the error bars are generally not visible due to the plotted point size being larger). For each line ratio, we used the highest resolution possible (indicated in the upper-left corner of the panel). To convert to $\Sigma_{\rm mol}$, which we provide for comparison on the top x axis of each panel, we assume a constant $R_{21} = 0.89$. We note that the x and y axes are correlated if the ^{12}CO (2−1) emission is used in the line ratio. The stacked points allow us to probe the line ratios in fainter regions, which sometimes confirms the trend suggested by the individual (significantly detected) sight line measurements (e.g. the ^{12}CO (2−1)/(1−0) in the top panel row) and sometimes reveals trends that could not be identified from the sight line measurements (e.g. the trend in the ^{12}CO (3−2)/(2−1) ratio in the second row).

4.2.2. Different CO isotopologue – fixed-J transition

Looking at different CO isotopologue line ratios with fixed rotational transitions can give insight into various physical quantities such as the abundance of the molecule or its optical depth, depending on whether the emission line is optically thin or thick (Davis 2014; Jiménez-Donaire et al. 2017b; Cormier et al. 2018). Figures 7 and 8 show CO line ratios for different CO isotopologues but at fixed-J transition. The ^{13}CO/^{12}CO line ratio shows for both the (1−0) and (2−1) transition the same significant correlation with galactocentric radius (negative), ^{12}CO brightness temperature (positive) and TIR surface brightness (positive). The (1−0) line ratio shows also indication of an enhancement in the centre of the galaxy of order 20% (see also centre right panel in Fig. 4). The C^{18}O/^{12}CO (1−0) line ratio shows a negative trend with galactocentric radius, but positive trends with ^{12}CO brightness temperature and TIR surface brightness. For the C^{17}O line, we only have two sight lines with significant detection at 34 arcsec resolution. We are very limited by the censored region and from the individual sightlines alone, we cannot infer any trends with radius, CO brightness and/or the TIR surface density. For C^{17}O/^{12}CO(1–0) we find an average value of ∼0.02, for C^{17}O/^{13}CO(1–0) ∼0.15, and for C^{17}O/C^{12}O(1–0) we find ∼0.7. Using stacking, we identify a positive trend with radius out to 4 kpc for the C^{17}O/^{12}CO(1–0), C^{17}O/^{13}CO(1–0) and C^{17}O/C^{18}O(1–0) ratios. Since the individual sightlines are affected by the censoring, we also provide the average line ratios using the stacked spectra: For stacked C^{17}O/^{12}CO(1–0) we find 0.009 ± 0.002, for the stacked C^{17}O/^{13}CO(1-0) we have 0.07 ± 0.03 and for the stacked C^{17}O/C^{18}O(1–0) we measure 0.4 ± 0.1.

4.2.3. Comparing different CO line ratios

As previously highlighted, different CO line ratios trace different gas characteristics and physical properties, depending on the

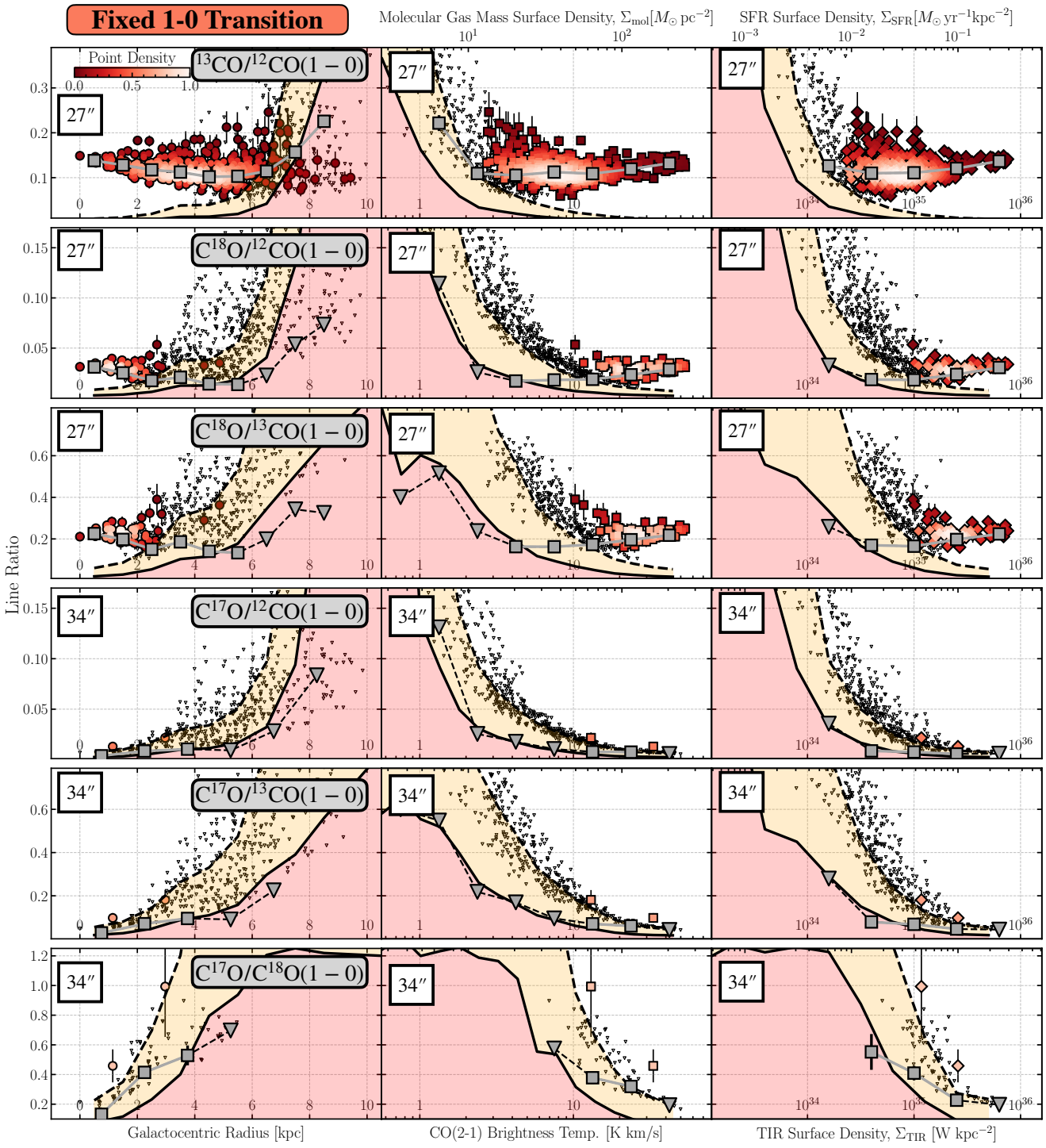

Fig. 7. CO line ratios with a fixed (1−0) transition but different CO isotopologues. For a description of the panels, see Fig. 6.

optical depth of the two lines. By comparing different line ratios that trace different conditions (e.g. the optical depth or the chemical abundance), we can gain insight into the relation between various physical conditions. Figure 9 shows a corner plot comparing different CO isotopologue line ratio combinations against each other. Plotted are the individual sight lines that show significantly detected line ratios in both axes, as well as the 50% and 75% inclusion contours using a kernel density estimation (KDE). We note that we do not account for censoring effects that can affect the wider distribution of the data points. To test for a linear correlation between the different line ratios, we computed the Pearson's r_p coefficient.

We do not find a clear linear trend for most combinations of line ratios at our working resolution of 1 to 2 kpc. A moderate trend ($|r_P| > 0.4$) of high significance ($p < 0.05$) can only be seen for $^{12}CO\,(2-1)/(1-0)$ versus $^{13}CO/^{12}CO\,(1-0)$, $^{12}CO\,(2-1)/(1-0)$ versus $C^{18}O/^{12}CO\,(1-0)$ and $^{13}CO/^{12}CO\,(1-0)$ versus $C^{18}O/^{12}CO\,(1-0)$ (ratio comparisons in question are marked in Fig. 9). However, these are the combinations that both have the $^{12}CO\,(1-0)$ line in the

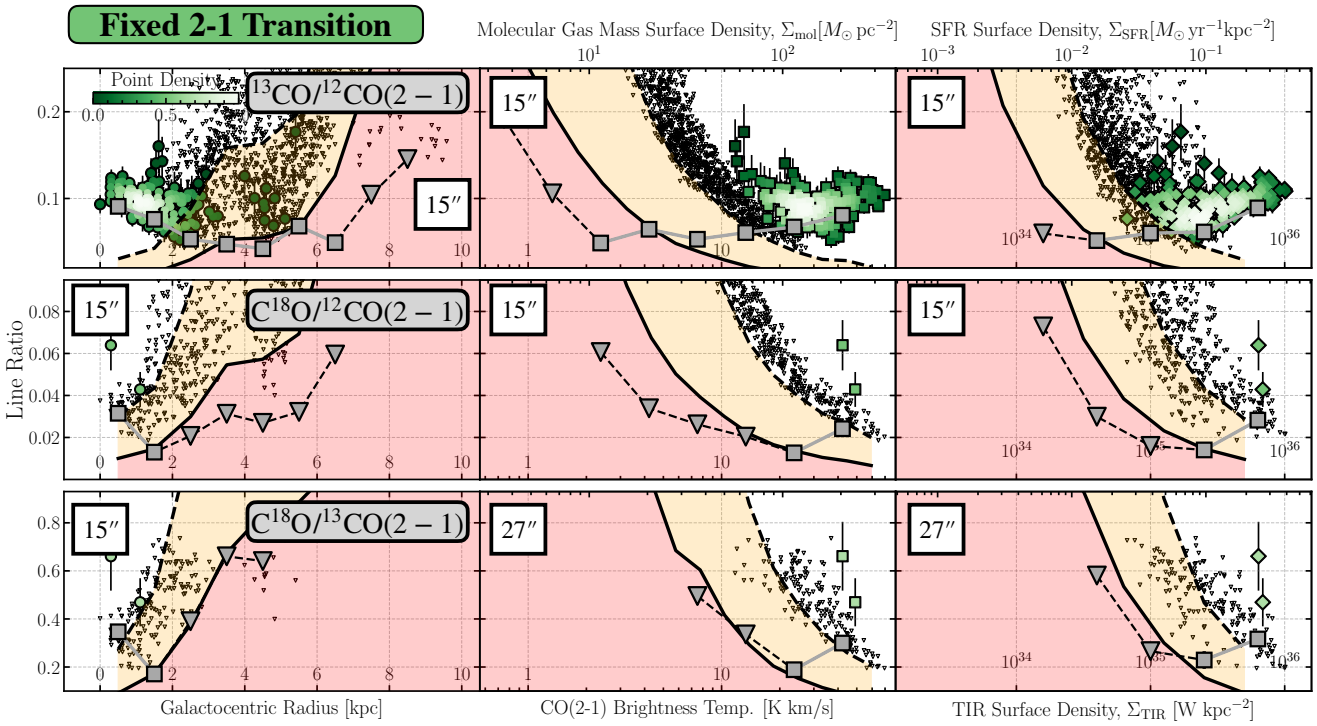

Fig. 8. CO line ratio with a fixed (2−1) transition but different CO isotopologues. For a description of the panels, see Fig. 6.

Table 5. Mean values and Kendall's τ rank correlation coefficient (p-value given in parentheses).

	Line Ratio	$\langle R\rangle$	$\langle R\rangle^{equal}$	Kendall's τ rank correlation coefficient		
				Radius	$W_{CO\,(2-1)}$	Σ_{TIR}
		(1)	(2)	(3)	(4)	(5)
	$^{12}CO\,(2-1)/(1-0)$	$0.89^{+0.11}_{-0.07}$	$0.9^{+0.3}_{-0.1}$	−0.20 (0.82)	−0.6 (0.14)	−0.6 (0.23)
	$^{12}CO\,(3-2)/(2-1)$	$0.37^{+0.09}_{-0.11}$	$0.32^{+0.10}_{-0.09}$	−0.80 (0.083)	1.0 (0.003)	1.0 (0.083)
	$^{13}CO\,(2-1)/(1-0)$	$0.61^{+0.09}_{-0.08}$	$0.61^{+0.10}_{-0.08}$	−0.80 (0.083)	−0.2 (0.7)	1.0 (0.083)
	$C^{18}O\,(2-1)/(1-0)$	$0.87^{+0.24}_{-0.15}$	$1.0^{+0.2}_{-0.2}$	–	–	–
fixed-J $1\rightarrow0$	$^{13}CO/^{12}CO$	$0.12^{+0.02}_{-0.02}$	$0.12^{+0.02}_{-0.02}$	−1.0 (0.017)	0.6 (0.13)	0.40 (0.48)
	$C^{18}O/^{12}CO$	$0.031^{+0.004}_{-0.006}$	$0.031^{+0.004}_{-0.008}$	−0.80 (0.083)	1.0 (0.017)	0.67 (0.33)
	$C^{18}O/^{13}CO$	$0.23^{+0.02}_{-0.03}$	$0.23^{+0.02}_{-0.03}$	−0.80 (0.083)	0.80 (0.083)	0.67 (033)
	$C^{17}O/^{12}CO$	–	–	1.0 (0.3)	–	−1.0 (0.33)
	$C^{17}O/^{13}CO$	–	–	1.0 (0.3)	–	−1.0 (0.33)
	$C^{17}O/C^{18}O$	–	–	1.0 (0.3)	–	−1.00 (0.33)
fixed-J $2\rightarrow1$	$^{13}CO/^{12}CO$	$0.09^{+0.01}_{-0.02}$	$0.09^{+0.02}_{-0.02}$	−1.0 (0.017)	0.73 (0.056)	1.0 (0.083)
	$C^{18}O/^{12}CO$	$0.034^{+0.006}_{-0.008}$	$0.034^{+0.008}_{-0.005}$	–	–	–
	$C^{18}O/^{13}CO$	$0.36^{+0.06}_{-0.06}$	$0.33^{+0.08}_{-0.04}$	–	–	–

Notes. They are measured for the line ratios of stacked spectra as a function of galactocentric radius, CO (2−1) brightness temperature, and TIR surface brightness (see Figs. 6, 7, and 8). Only stacked points with $S/N > 5$ are considered. A dash indicates that only two or fewer significant measurements exist for the specific line ratio. (1) $\langle R\rangle$ indicates the average line ratio weighted by $^{12}CO\,(2-1)$ brightness temperature (see Eq. (8)). The uncertainty for each line ratio is given by the weighted 16th and 84th percentiles. (2) The volume weighted median line ratio and 16th and 84th percentiles (since all pixel have the same size, this corresponds to weighing all points equally). (3) For the correlation coefficient computation, we only include stacked points at $r_{gal} < 5$ kpc. (4) Only includes stacked points with $W_{CO\,(2-1)} > 2$ K km s^{-1}. (5) The correlation coefficient computation does not include any additional constraints.

denominator. Consequently, the trends may hint more at a correlation between the two numerators. Such trends are expected, given that all CO isotopologues have a similar spatial distribution within the galaxy, so we expect a correlation in the strength of their emission. For all other combinations, no significant linear trend can be determined.

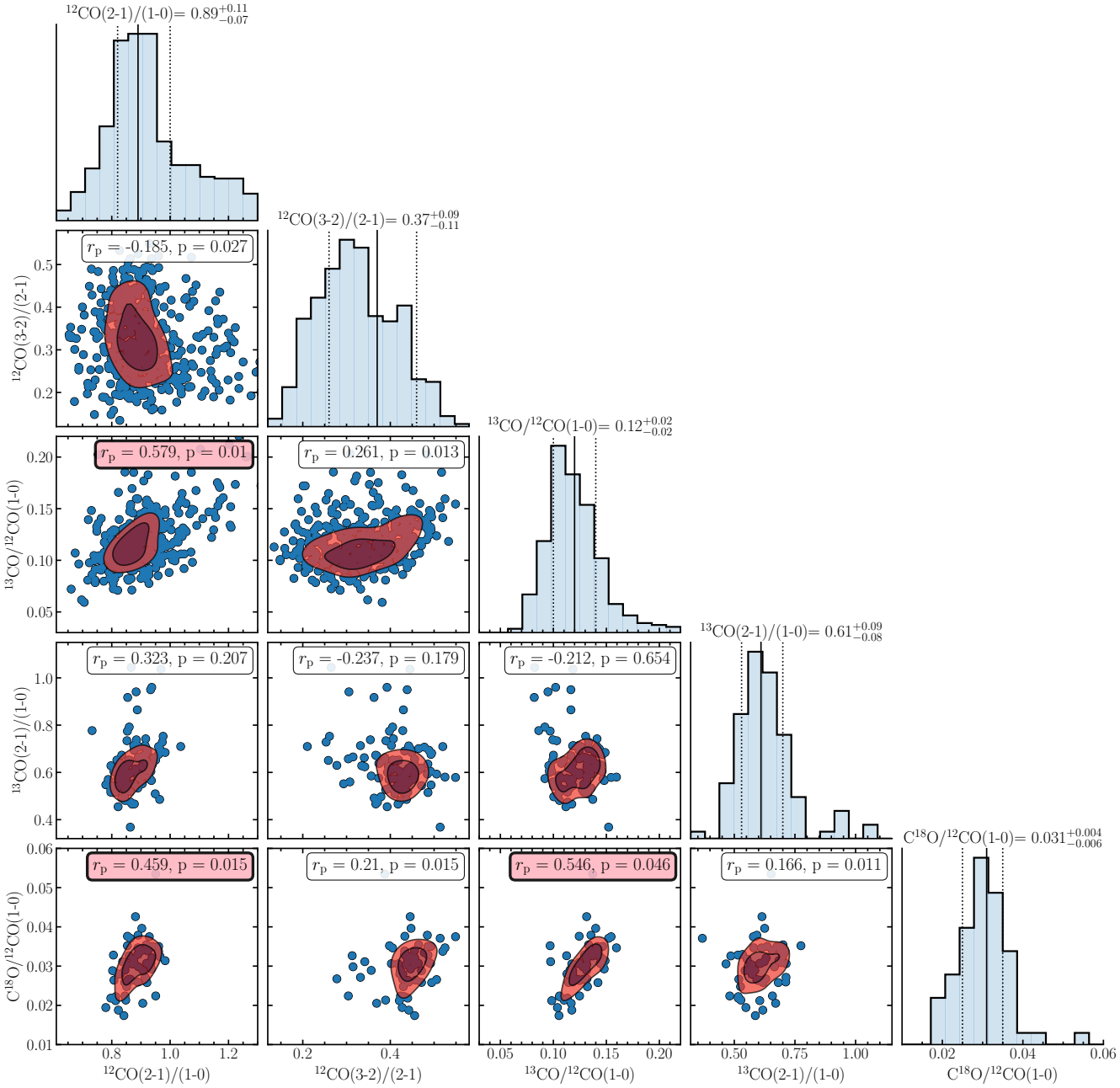

Fig. 9. Comparing different CO line ratios against one another at 27 arcsec. Individual sight lines and significantly detected CO line ratios vs. other line ratios are shown. Contours show the 50% and 75% inclusion region based on a KDE. For each line ratio comparison, Pearson's r_P correlation coefficients and its p-value are indicated in the panel. The histograms indicate the distribution of each line ratio using all significant data points. The CO (2−1) weighted mean and weighted 16th and 84th percentiles are also shown. We find a moderate, significant linear correlation ($|r_P| > 0.4$ and $p < 0.05$; panel labels are colour-coded in the case of a moderate linear correlation) for ratio comparison in panels (b), (g), and (i) only.

4.3. Line ratios and the galactic environment

For several CO line ratios, an enhancement towards the centre of the galaxy is observed (see Sect. 4.2). To analyse whether galaxy morphological features, such as the galactic centre, spiral arms or interarm regions, have an impact on the molecular gas properties, we classify each sight line as centre, spiral arm, interarm or general disc (see Fig. 10). This classification is based on visual inspection of optical HST data as well as the extent of the ^{12}CO (2−1) emission. In our study, the 'centre' refers to the central ($r_{gal} \leq 45$ arcsec $\approx$2 kpc) region of the galaxy.

Figure 11 shows histograms of the CO line ratio distributions for ^{12}CO (2−1)/(1−0), ^{12}CO (3−2)/(2−1) and ^{13}CO (2−1)/(1−0), separated by the different environments. These three line ratios show significant pixel detections in the centre, spiral arm and interarm regions. The numerical values of the mean and 16th and 84th percentiles for each environment are given in Table 4. We find again that all three line ratios show higher values in the central region, but this enhancement is significant only in the case of ^{12}CO (3−2)/(2−1). Furthermore, we find evidence for a difference in the line ratios between arm and interarm regions for ^{12}CO (2−1)/(1−0) and ^{12}CO (3−2)/(2−1). We note that the line ratios in the interarm regions are higher for ^{12}CO (2−1)/(1−0) and lower for ^{12}CO (3−2)/(2−1) than the spiral arm regions. For the ^{13}CO/^{12}CO (1−0) line ratio, we also find a larger average

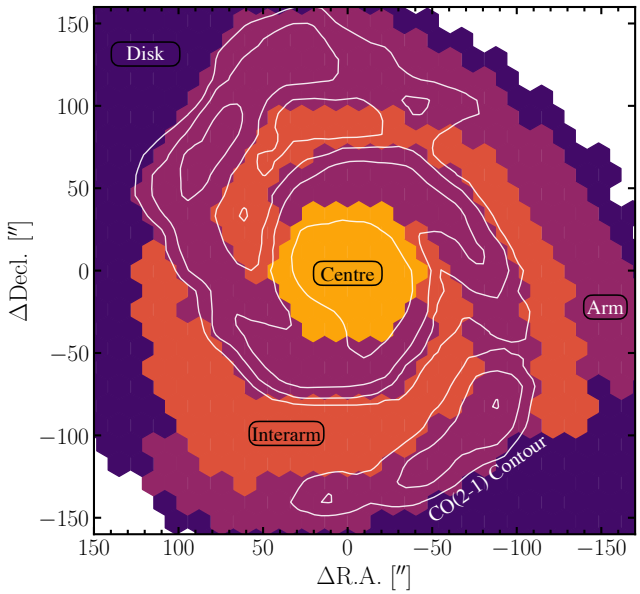

Fig. 10. Environmental mask of M 51. Based on a visual inspection of optical HST data and ^{12}CO (2−1) emission, we generated the following environmental mask. The pixels are colour-coded by their associated region. This includes the centre (bright orange), interarm (dark orange), spiral arm (magenta), and disc (purple). The centre includes data points within a 45 arcsec aperture. White contours indicate ^{12}CO (2−1) emission at 7, 10, 15, and 30 K km s^{-1}.

value in the interarm ($0.12^{+0.03}_{-0.02}$) than in the spiral arm region ($0.11^{+0.01}_{-0.02}$), though the two medians lie within the margin of error of each other.

4.4. Spiral arm and interarm variations

In the following section, we further investigate the arm-interarm contrast, as it stands against previous studies, which found a larger ^{12}CO (2−1)/(1−0) line ratio in the spiral arm region than the interarm region (Koda et al. 2012). To further study the systematic variations in the ^{12}CO (2−1)/(1−0), ^{12}CO (3−2)/(2−1), and ^{13}CO/^{12}CO (1−0) line ratios across the spiral arm and interarm regions, we use a similar approach as described in Koda et al. (2012). The method is illustrated for the ^{12}CO (2−1)/(1−0) line ratio in Fig. 12, while a comparison of all four line ratios is shown in Fig. 13. The data are binned using logarithmic spirals, which are described by

$$r = \mathrm{e}^{k\cdot\psi}, \tag{12}$$

where $k \equiv \tan(\theta)$ with the pitch angle θ and the spiral phase ψ. For M 51, we use a pitch angle[11] of $\theta = 20°$. Each segment spans over 40° and we increment in steps of $\Delta\psi = 20°$ anti-clockwise. For the analysis, we exclude the central ($r_{\rm gal} \leq 45$ arcsec) region and only bin points with $S/N > 5$. The logarithmic spiral segments can be seen in the left and central panels of Fig. 12. The red and blue lines indicate the molecular spiral arms (ψ = 40°−100° and 220°−290°). We note that the shaded regions in the upper-right and bottom-left corners are also excluded, as there the molecular arm starts to deviate significantly from a simple logarithmic spiral.

The right panel of Fig. 12 shows the result of the line ratios binned by spiral phase angle. The two spiral arms are based on molecular gas emission. The figure shows the binned arithmetic average of each logarithmic spiral arm segment. Using the same data, we can confirm the larger ^{12}CO (2−1)/(1−0) line ratios in the interarm regions compared to the arm regions found by den Brok et al. (2021). The average line ratio in the central segment of the molecular arm region is 0.85, while in the interarm region the average is ∼0.93. We note that the enhancement of the line ratio in the interarm is more concentrated towards the downstream, convex part of the spiral region. A similar variation is also seen in the ^{13}CO/^{12}CO (1−0) ratio (see Fig. 13). We note that Table 4 also lists the line ratios separated into arm and interarm. But the value in the table are ^{12}CO (2−1) weighted and combine data points spanning a wider range of spiral phases. Consequently, we concentrate the analysis of the azimuthal variation on the analysis plotting the line ratios as a function of the spiral phase.

To make sure the trend we find is not due to higher line ratios at larger radii, we vary the S/N threshold and also add a constraint to only include sight lines within a given galactocentric radius. The results are shown in Fig. 14, where besides the $S/N > 5$ threshold (which is used in Fig. 12), we also include thresholds of $S/N > 10, 15, 20$. For the radial thresholds, we include $r_{\rm gal} < 6, 5, 4$ kpc. We see that the finding of larger ^{12}CO (2−1)/(1−0) line ratios in the interarm region is independent of the threshold implemented.

We note that in particular the 3 mm lines in the interarm region are subject to significant error beam contribution, which to some degree can drive the larger ^{12}CO (2−1)/(1−0) line ratio in the interarm region. We discuss the effect in more detail in Appendix A.

5. Discussion

The rich dataset of different CO isotopologues allows us to address a multitude of science questions. First, in Sect. 5.1 we look at the various trends we find in the CO isotopologue line ratios. We compare them to the literature and then, in Sect. 5.4, investigate what the observed trends in the line ratios may imply. In Sect. 5.1 we also look into a particular environmental variation in the line ratio – the arm–interarm differences we find most notably in the ^{12}CO (2−1)/(1−0) line ratio – and constrain the cause for this variation. The galactic environment appears to have an impact on the line ratio, so we also investigate how environment affects the CO spectral line energy distribution (SLED) in Sect. 5.5.

5.1. Comparing R_{21} with previous studies

The first questions to address are whether the galaxy M 51 conforms to the trends seen in other galaxies regarding the CO line ratios and what we can learn from such trends. When looking at the ^{12}CO line ratios, a few peculiarities are evident for M 51. The well-studied line ratio of ^{12}CO (2−1)/(1−0) (denoted hereafter as $R_{21}^{^{12}\rm CO}$) is rather high, with a luminosity-weighted average value of $R_{21}^{^{12}\rm CO} = 0.89^{+0.11}_{-0.07}$. The question of how this compares to findings from other studies using different datasets then arises. In their ^{12}CO line ratio study, comparing literature values of a larger set of spiral disc galaxies, den Brok et al. (2021) found a common

[11] To be consistent with the study of Koda et al. (2012), we used the value of 20° for the pitch angle. This value is similar to the value of 21.°1 given by Shetty et al. (2007) and the value of 18.°5 found in Pineda et al. (2020).

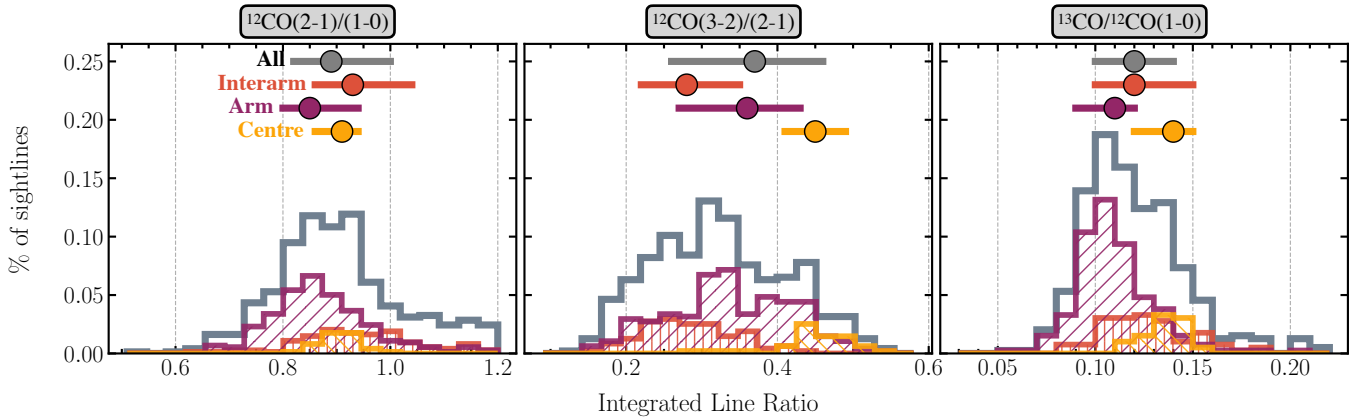

Fig. 11. Distributions for three selected CO line ratio in different galactic environments. The locations of the various galactic regions are shown in Fig. 10. For each region, the CO (2−1) brightness temperature weighted median (see Eq. (8)) is indicated by the circle and the 16th and 84th percentile range by the bars. The numerical values are given in Table 4. For the ^{12}CO (2−1)/(1−0) line ratio, we find evidence of larger values in the interarm than in the spiral arm. For ^{12}CO (3−2)/(2−1) we find the opposite trend. ^{12}CO (3−2)/(2−1) and ^{13}CO/^{12}CO (1−0) show a clear enhancement of the line ratio in the galaxy centre.

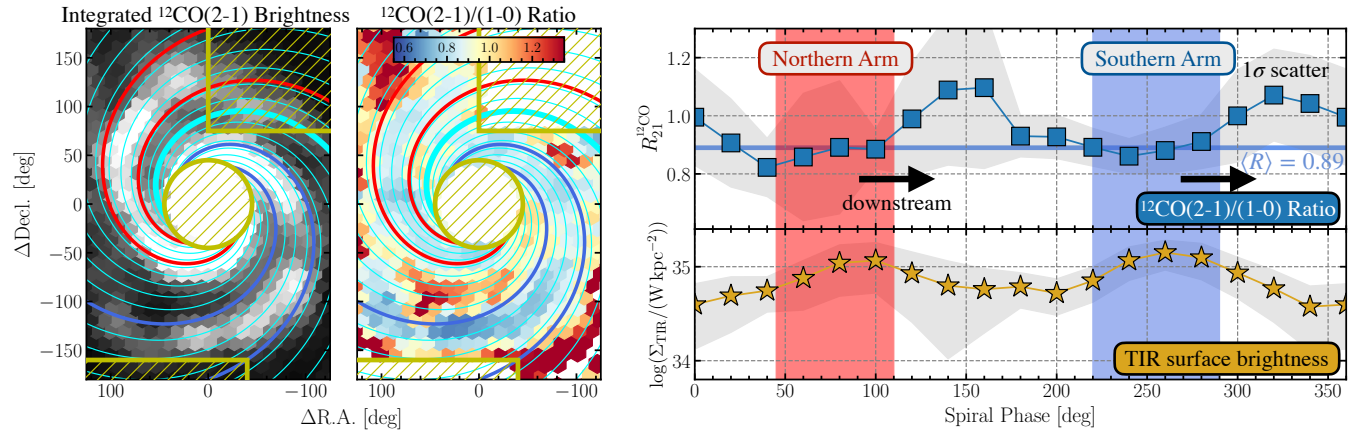

Fig. 12. Spiral arm–interarm CO line ratio variation. This figure closely follows the layout of Fig. 4 in Koda et al. (2012). *Left*: ^{12}CO (2−1) brightness temperature map with the logarithmic spiral pattern. The logarithmic spiral has a pitch angle of 20°. The bold cyan line indicates the starting spiral phase (ψ = 0°). The spiral phases increase anti-clockwise in 20° increments. The red and blue spirals indicate the bounds of the molecular gas spiral arm (at ψ = 45°−110° and 220°−290°). We ignore the top-right and bottom-left regions, where the molecular arm deviates from the logarithmic spiral pattern, in our analysis. Furthermore, we exclude the central region (radius of 45 arcsec, indicated by the yellow hashed region). *Centre*: ^{12}CO (2−1)/(1−0) line ratio map. We only show sight lines at $S/N > 5$ and not within the exclusion regions. *Right*: Average line ratio for each spiral phase bin on top (which has a width of 40° and increases by 20° every step). The blue horizontal line shows the galaxy-wide, luminosity weighted median line ratio of $\langle R_{21}^{^{12}\mathrm{CO}} \rangle$. The bottom panel shows the TIR surface density (which is proportional to the SFR surface density) to highlight the spiral arm. The grey shaded area indicates the standard deviation. The locations of the northern (red) and southern (blue) spiral arm are indicated. The downstream direction of the spiral arm is indicated by the black arrow.

line ratio of $R_{21}^{^{12}\mathrm{CO}} = 0.59 \pm 0.1$, making the line ratio we find for M 51 clearly stand out. Similarly, Leroy et al. (2022), studying the low-J ^{12}CO line ratios using single-dish CO mapping surveys and the Physics at High Angular resolution in Nearby Galaxies (PHANGS) survey find a mean value and respective 16th and 84th percentile of $R_{21}^{^{12}\mathrm{CO}} = 0.65^{+0.18}_{-0.14}$. Other studies that investigated this line ratio in M 51 found lower global values. Koda et al. (2012) found an average value of $R_{21}^{^{12}\mathrm{CO}} \approx 0.7$, but they identified enhanced values in the spiral arm regions that are closer to our mean value. Vlahakis et al. (2013) also investigated the spatial variation in the ^{12}CO line ratios in M 51. They found an overall higher median $R_{21}^{^{12}\mathrm{CO}}$ of 0.8, which is close to our luminosity-weighted value.

In Fig. 12, we study the spatial variation in the ^{12}CO (2−1)/(1−0) line ratio across the arm and interarm regions of M 51. The main result is the higher line ratios in the interarm regions (∼0.93) as opposed to the arm regions (∼0.85), as also seen in Table 4. This trend stands against previous findings from, for example, Sakamoto et al. (1997), who found the opposite trend in the Milky Way. Koda et al. (2020) reported higher line ratios in arm as opposed to interarm regions for the spiral galaxy M83. In fact, Koda et al. (2012) and Vlahakis et al. (2013) (using the same data) studied the arm–interarm variation in M 51 and found opposing trends with respect to this study.

We investigated in detail the origin of this discrepancy of the arm–interarm variation in den Brok et al. (2021). The study by Koda et al. (2012) used different CO (1−0) and CO (2−1) data than used here. Their CO (2−1) data were taken from the HERACLES survey (Leroy et al. 2011b), and the CO (1−0) data came from the Nobeyama Radio Observatory (NRO) observations (Koda et al. 2011). Performing the same analysis as shown

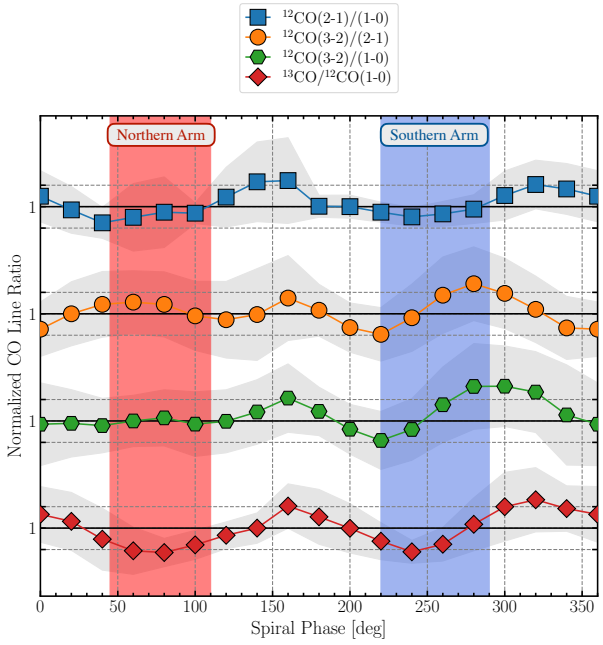

Fig. 13. Spiral arm–interarm line ratio variations for three different CO line ratios. We only include sight lines with $S/N > 5$ for each of the emission lines of the respective line ratio. We use a working resolution of 27 arcsec. We normalise the line ratio by the median value. The horizontal grey dotted lines indicate ±15% deviations from the median value.

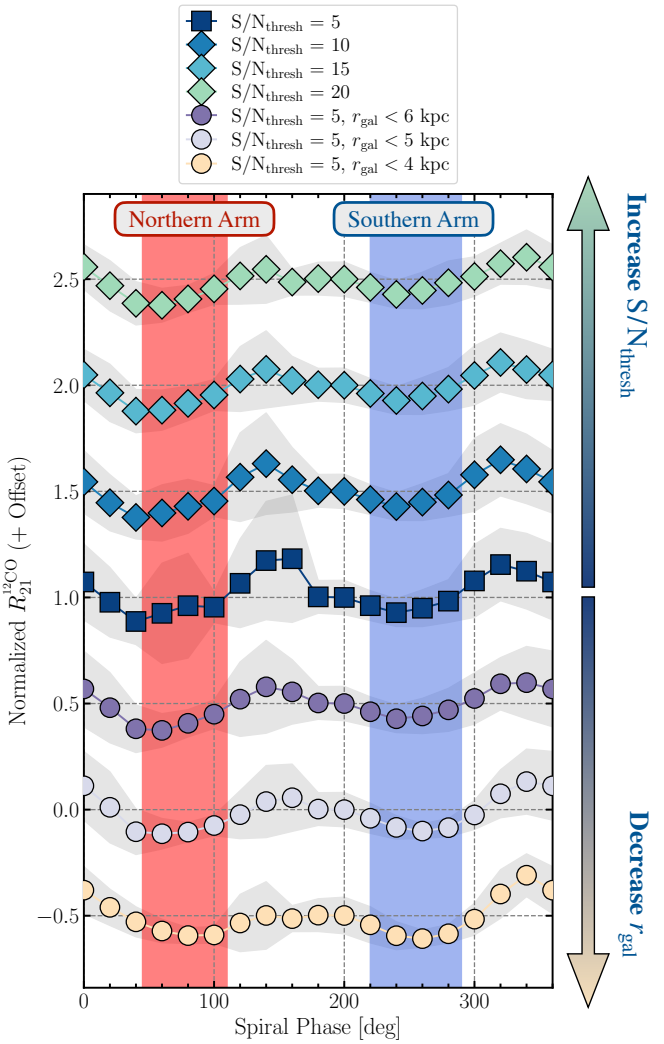

Fig. 14. Spiral arm–interarm CO line ratio variation consistency. For the arm–interarm variation in Fig. 12, we include all sight lines with $S/N > 5$. Here, we increase the S/N threshold from 5 to 20 in steps of 5 to investigate whether the higher line ratios are still preserved in the interarm region. Furthermore, we add a radial constraint, only including sight lines within a given galactocentric radius of 4, 5, and 6 kpc. We normalise the line ratios by the global CO (2−1) brightness weighted median. We offset different line ratios in steps of 0.5 (in the positive direction for increasing S/N and in negative steps for decreasing radial constraint). We see that the trend of higher line ratios in the interarm region is persistent for all computations shown in this figure.

in Fig. 12 for all the different combinations of the CO (1−0) and CO (2−1) datasets, den Brok et al. (2021) found that the cause of the discrepancy comes from substituting the CO (1−0) data and not from substituting CO (2−1) data. This demonstrates that the opposite arm–interarm trend is not an artefact of the new CO (2−1) data taken with the IRAM 30 m telescope as part of this programme and that care should be taken combining datasets from different telescopes and receivers when carrying out measurements of molecular line ratios.

To verify if using ^{12}CO (2−1) with a different sensitivity and flux calibration uncertainty changes the outcome, we substituted the CLAWS CO (2−1) data with the HERACLES CO (2−1) data (Leroy et al. 2009) as an experiment. We also find a lower line ratio ($R_{21}^{^{12}CO} \approx 0.7$; see Appendix B). Such a dependence of the absolute value on the specific dataset has been discussed in den Brok et al. (2021) by comparing HERACLES, ALMA, IRAM 30 m, and NRO CO (1−0) and CO (2−1) data. A variation of order 20% has been found between observations of the same line from different telescopes. This variation is attributed to uncertainties in the absolute flux calibration of the individual telescopes, which can vary between 5% to 20%. However, the flux calibration generally affects the observational data globally, so while the absolute values may differ, we would not expect to find different galaxy-wide trends when comparing CO ratios using different single-dish telescope data (e.g. den Brok et al. 2021 find the same arm–interarm $R_{21}^{^{12}CO}$ (i.e. higher values in the interarm region relative to the arm region) trend in M 51 when substituting CLAWS with HERACLES data).

The discrepancy could also be explained due to instrumental reasons. As previously mentioned, uncertainties in the absolute flux calibration of order up to 20% can lead to differences in the absolute value found when comparing observations from different telescopes and/or observing runs. Such variations are, however, expected to lead to global differences, so we do not expect local variation. Furthermore, contributions from the error beam might significantly affect the detected emission, in particular when observing interarm positions, if emission from brighter spiral arm regions enters via the error beam. In Appendix A, we investigate these effects for this survey and show that we still find the same arm–interarm trend even when taking account of these instrumental effects.

The CO (2−1)/(1−0) line ratio is a tracer of both the gas density and excitation temperature. There is strong evidence that interarm regions do not host higher-density molecular gas (Sun et al. 2020). Consequently, a higher line ratio in interarm regions would indicate the presence of molecular gas with a higher excitation temperature. If the UV and optical attenuation is lower in a certain region, one can assume that the gas is

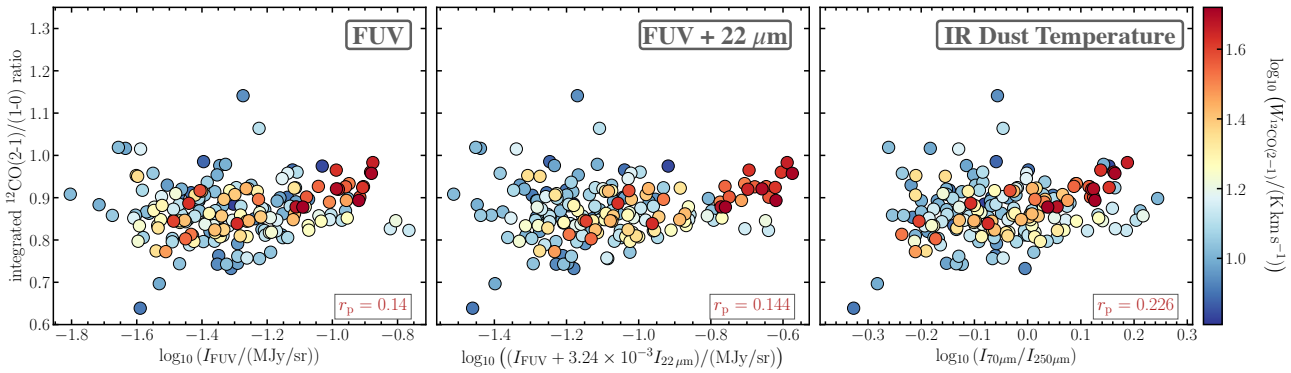

Fig. 15. ^{12}CO (2−1)/(1−0) line ratio compared to FUV intensity (*left*), FUV+22 μm (*centre*), and infrared colour (*right*). We only include sight lines with $S/N > 5$ for the line ratio to minimise scatter from faint ^{12}CO lines. We use a working resolution of 27 arcsec. FUV emission follows to some extent young (≤100 Myr) stellar populations. Because FUV can be heavily obscured, we correct using 22 μm data from *WISE* band-4 observations. To combine FUV and 22 μm, we multiply the 22 μm by a factor 3−24 × 10^{-3}. The resulting sum is proportional to the SFR surface density (Leroy et al. 2019). The infrared 70 μm/250 μm colour is a proxy for the dust temperature. We provide the Pearson's linear correlation coefficient, r_p, in each panel. We do not find any evident correlation of the line ratio with either quantity.

less shielded and the molecular gas can reach higher excitation temperatures, producing a higher line ratio. By contrast, regions with higher-density gas are better shielded and thus showing a lower excitation temperature. We note, however, that Koda et al. (2020) did not exclusively found larger line ratios in spiral arm regions in M83. To be more precise, they found larger $R_{21}^{^{12}CO}$ ratios towards the downstream, convex part of the spiral arm, spanning into the interarm region (see Fig. 1 in Koda et al. 2020). We also find enhanced line ratios more towards the downstream, convex part of the spiral arm. Further, they postulated that there is a direct or indirect link between dust heating via the ISRF and molecular cloud conditions, which may explain the trend. The large CO line ratio could then potentially be explained due to the evolution of massive stars after leaving the spiral arm downstream and consequently contributing more heavily to the dust heating because they are no longer obscured by their birth cloud. Based on the timescales of this evolution, we would expect the location to vary within spiral arm and interarm regions. Looking at Fig. 15, we do not find any apparent global correlation between FUV and the sum[12] FUV+22 μm with dust colour or $R_{21}^{^{12}CO}$. Consequently, the explanation provided by Koda et al. (2020) for the M83 is at least not straightforward to apply to explain the arm–interarm line ratio variations observed in M 51. Alternatively, the presence of diffuse emission can impact the line ratio. The result of a lower $R_{21}^{^{12}CO}$ in the spiral arm region could suggest the presence of a diffuse CO gas component, which boosts the ^{12}CO (1−0) emission (Cormier et al. 2018). Such a diffuse component would be in accordance with the diffuse component found by Pety et al. (2013).

5.2. Interpreting variations in other line ratios

For the ^{12}CO (3−2)/(2−1) line ratio, Vlahakis et al. (2013) found a global value of $R_{32}^{^{12}CO} = 0.5 \pm 0.14$, which is higher than the value we find ($R_{32}^{^{12}CO} = 0.37^{+0.09}_{-0.11}$), but within the margin of error. Similar to our finding, they identified a trend of larger values in the arm (0.5) than in the interarm (0.4), but their absolute values again are higher than the values we find.

Due to the high sensitivity of the observations we also significantly detect C^{17}O (1−0) emission towards the centre of the galaxy, if we use the 34″ spatial resolution data (see Fig. 7). While we find a positive trend with the galactocentric radius for the C^{17}O/^{12}CO (1−0), C^{17}O/^{13}CO (1−0), and C^{17}O/C^{18}O (1−0) ratios, we note the caveat that this could also be an artefact due to the fact that they are constrained by data points within the censored region. For C^{17}O/C^{18}O (1−0), when stacking by radius, we find an average value of 0.4 ± 0.1. This is slightly larger than, but of similar order of, the value of 0.24 ± 0.01 found for the solar neighbourhood (Wouterloot et al. 2005).

We also compared the azimuthal trend for the ^{12}CO (3−2)/(2−1) ^{12}CO (3−2)/(1−0), and ^{13}CO/^{12}CO (1−0) line ratios. We select these line ratios because we already investigated them in Fig. 11. For all three line ratios in Fig. 13, we only include sight lines that have $S/N > 5$ for both lines for each spiral phase. We notice that particularly the ^{13}CO/^{12}CO (1−0) line ratio clearly shows larger values in interarm regions compared to spiral arm regions. Again, such a trend could be attributed to either an increased ^{13}CO abundance or variation in the optical depth of the gas. Based on our discussion in Sect. 5.4, in which we argue that ^{13}CO abundance variations cannot explain the variation in the different CO isotopologue line ratios, we therefore conclude that most likely changes in the optical depth explain the observed difference in the arm–interarm values for the ^{13}CO/^{12}CO line ratio.

The ^{12}CO (3−2)/(2−1) line ratio also shows clear azimuthal variations. We see that the line ratio also peaks in the interarm region at spiral phase of ∼150° (see Fig. 13). We note that from the lines analysed in the figure, it is the only one that does not have ^{12}CO(1-0) in the denominator. The fact that the line ratio also peaks in the interarm region further underlines the presumption that the discrepancy to previous results comes from the use of different ^{12}CO(1–0) datasets (PAWS and NRO; see discussion in Sect. 5.1). But for ^{12}CO (3−2)/(2−1), the line ratio value also peaks in the spiral arm regions. Vlahakis et al. (2013) attributed the larger values in spiral arm compared to interarm regions to the presence of warmer and/or denser molecular gas. This is consistent with the detection of HCN (1−0) in spiral arms (Querejeta et al. 2019), but it does not explain the opposite trend for the ^{12}CO (2−1)/(1−0) line ratio. We have also seen opposite stacked ^{12}CO (3−2)/(2−1) ratio trends with galactocentric radius, ^{12}CO (2−1) brightness temperature, and TIR surface brightness when comparing to stacked ^{12}CO (2−1)/(1−0) ratio trends (see Fig. 6). This could be explained by the fact that, because of its higher excitation, ^{12}CO (3−2) emission is more

[12] We use *WISE* band-4 22 μm observations. For the sum, we normalise the infrared intensity by a factor 3.24 × 10^{-3}. The resulting sum is proportional to the SFR surface density (Leroy et al. 2019).

constrained to denser regions within the molecular gas and the detected emission does not have a large diffuse component.

In Fig. 9, we compare different CO line ratios with one another. We do not find any clear ratio-to-ratio trends. We recognise that in particular noise effects and uncertainties (e.g. flux calibration uncertainty) can wash out any minor existing trends. Furthermore, due to the censoring effect of line ratios with a low value, potential correlations could non-trivially be suppressed in this analysis.

5.3. Comparing CO line ratios to simulations

To better understand what we can learn from specific CO isotopologue lines, we compare our findings to simulations. Peñaloza et al. (2017) studied the utility of the ^{12}CO (2−1)/(1−0) line ratio for uncovering the physical and chemical properties of molecular clouds. In their study, they carried out a high resolution smoothed particle hydrodynamics (SPH) simulation of an isolated molecular cloud using the `GADGET-2`) SPH code supplemented with a model for the time-dependent H_2 and CO chemistry. The results of this simulation were resampled onto a hierarchical Cartesian mesh and then post-processed with the `RADMC-3D` radiative transfer code (Dullemond et al. 2012) to generate synthetic maps of ^{12}CO (2−1) and (1−0) line emission. We note that the spatial resolution used in the study is on parsec scale, while our observations are on kiloparsec scales. Consequently, any comparison has to be taken with caution, since differences in the spatial scale can also impact the relations. Peñaloza et al. (2017) found a bimodality in $R_{21}^{^{12}\mathrm{CO}}$, with one peak at ∼0.4 and another one at ∼0.7, which are below the value we see (∼0.89). They attributed the high peak to emission from cold ($T \leq 40$ K) and denser ($n \geq 10^3$ cm^{-3}) molecular gas, and the lower peak to faint emission from warmer ($T \geq 40$ K) and diffuse ($n \leq 10^3$ cm^{-3}) molecular gas. We do not see such a bimodality in $R_{21}^{^{12}\mathrm{CO}}$ (see e.g. Fig. 5). However, we cannot resolve individual giant molecular clouds with our resolution (27 arcsec or ∼1–2 kpc). As the lower ratio peak comes from diffuse emission, we would need high sensitivity observations for a secure detection of this component and high spatial resolution to separate it from molecular clouds. In a follow-up study, Peñaloza et al. (2018) investigated the impact of the galactic environment on 'cloud-averaged' CO line ratios $R_{21}^{^{12}\mathrm{CO}}$ and $R_{32}^{^{12}\mathrm{CO}}$. They performed simulations similar to Peñaloza et al. (2017), but involving a much broader range of model clouds, and analysed the post-processed CO emission. For $R_{32}^{^{12}\mathrm{CO}}$, they reported larger values (∼0.6) than what we find (∼0.4). However, their inferred scatter is ±0.2 for both $R_{21}^{^{12}\mathrm{CO}}$ and $R_{32}^{^{12}\mathrm{CO}}$ when averaging the line ratio over whole clouds. Based on their simulations, they suggested that the scatter is mainly driven by variations in the ISRF and the CRIR. Our data show a similar range of scatter, despite the large difference in spatial scale, so variations in the ISRF and CRIR could be a potential explanation for the observed change in $R_{21}^{^{12}\mathrm{CO}}$ and $R_{32}^{^{12}\mathrm{CO}}$.

The ratios of $R_{21}^{^{12}\mathrm{CO}}$ and $R_{32}^{^{12}\mathrm{CO}}$ across galactic environments were also investigated in the recent study by Bisbas et al. (2021). They rely on 3D thermochemical simulations and synthetic observations of magnetised, turbulent, self-gravitating molecular clouds. They found a remarkably flat trend for both $R_{21}^{^{12}\mathrm{CO}}$ and $R_{32}^{^{12}\mathrm{CO}}$ with respect to several galactic parameters, such as CRIR, FUV emission, and metallicity. They suggested that the flat trend is mainly due to the fact that all the environmental factors they investigated affect the ^{12}CO transitions equally. Matching to this prediction, we do not find any significant systematic variation for $R_{21}^{^{12}\mathrm{CO}}$ (see Fig. 6). However, we see a clear negative trend with galactocentric radius and SFR surface density for $R_{32}^{^{12}\mathrm{CO}}$. Consequently, this hints at another driving factor besides changes in ISRF and CRIR. But we note that Bisbas et al. (2021) only simulated molecular clouds and not the diffuse medium, which could explain the observed discrepancy or it can again be attributed to the fact that in their study they used a much higher spatial scale (approximately parsec scales).

So far, we have only discussed ^{12}CO line ratios. In our further analysis, we now include the other CO isotopologue lines and study the impact of the galactic environment.

5.4. Implications from CO isotopologue line ratio trends

As discussed in the previous section, we find clear evidence for variations within the galaxy for several combinations of different CO isotopologue line ratios (see Figs. 6, 7 and 8). We remind as a caveat that our observations have a spatial resolution of ∼1–2 kpc. Consequently, we study beam-averaged emission, so sub-beam variations can play a role (see Sect. 5.6). In the subsequent discussion, we focus on the following line ratios: ^{12}CO (2−1)/(1−0), ^{13}CO (2−1)/(1−0), ^{13}CO/^{12}CO (1−0), C^{18}O/^{12}CO (1−0), and C^{18}O/^{13}CO (1−0).

There are several potential explanations for the observed variations and trends. In a study of the ^{13}CO/^{12}CO line ratio variations in a sample of early-type galaxies, Davis (2014) offers three major explanations for systematic changes in the line ratio between different isotopologues. Summarised, variations can be explained by (i) different excitation processes for the individual CO isotopologues, (ii) fractional abundance variations in ^{13}CO and C^{18}O relative to ^{12}CO, and (iii) changes in the optical depth of the gas for one of the CO isotopologues. We note that, while ^{12}CO is generally optically thick, ^{13}CO and C^{18}O are mostly optically thin (Cormier et al. 2018), so changes in abundance will impact the emission of these lines. Using data from our survey, we can, to first order, try to isolate the main driver for the observed line ratio variations.

CO is mainly excited to higher rotational states by collisions with H_2 or He, or through photon trapping (Narayanan & Krumholz 2014). We do assume that the excitation is subthermal for most parts of our observations. Because all CO isotopologues seem to trace the same spatial region at the spatial resolution of this study (∼20 arcsec/1 kpc) and because the ^{13}CO/^{12}CO (1−0) and (2−1) line ratios both exhibit negative trends with galactocentric radius and positive trends with CO brightness temperature and TIR surface brightness, it is unlikely that different excitation processes that we investigate in more detail below cause the observed variations.

Potential mechanisms that can cause variations in the relative fractional abundance of ^{13}CO and C^{18}O are selective photodissociation, chemical fractionation or selective nucleosynthesis. In a recent letter, Jiménez-Donaire et al. (2017b) argued that CO isotopologue trends with galactocentric radius and SFR surface density, found across a sample of nearby spiral galaxies, are consistent with fractional abundance variations expected due to fractionation. Chemical fractionation is a process that can enrich ^{13}CO, but it is highly temperature dependent (Watson et al. 1976; Keene et al. 1998) and favourable in cold conditions. This process occurs in cold regions, such as the outskirts of galaxies. If this were the main cause of the observed variations, we would find lower ^{13}CO abundances in warmer regions. Due to more heating from young stars, it is expected that the SFR surface density correlates to a certain degree with gas temperature. Consequently, we expect a decrease in ^{13}CO abundance

with increasing Σ_{SFR}. As $C^{18}O$ is not affected by fractionation, the decreasing radial trend that we find for the $^{13}CO/C^{18}O$ line ratio, is in agreement with this explanation. However, we also see an increasing trend with increasing Σ_{SFR} for the $^{13}CO/^{12}CO$ line ratio, which contradicts the explanation that abundance variations are due to chemical fractionation alone, as we would expect the opposite trend: A larger line ratio at larger radii and smaller SFR surface densities would be due to an increase in the abundance of ^{13}CO in these environments.

Additionally, selective photodissociation cannot explain the observed trend in $^{13}CO/^{12}CO$. The process occurs in strong ISRFs. While on the one hand, ^{12}CO more shielded, ^{13}CO on the other hand is less well protected over large areas, so strong UV radiation will destroy the molecule (van Dishoeck & Black 1988). As high star formation is linked to the presence of OB stars, a negative trend with SFR would have been expected. Abundance variations due to selective nucleosynthesis could explain the observed decreasing trend in the $^{13}CO/C^{18}O$ line ratio with SFR surface density. While ^{12}C and ^{18}O are mainly produced in massive stars, ^{13}C is primarily produced in low-mass stars (Sage et al. 1991), as it is converted further to ^{14}N in high-mass stars ($>8\,M_{\odot}$), which would lead to only a very small replenishing rate of ^{13}C in the ISM (Prantzos et al. 1996). But in low- and intermediate-mass stars ^{13}C can surface, due to convection, during the red giant phase and consequently enhance the abundance (Wilson & Matteucci 1992). In their study, Brown & Wilson (2019) attributed the extremely low $^{13}CO/C^{18}O$ line ratio in ULIRGs to an excess in massive star formation. Furthermore, an increase in $^{12}C/^{13}C$ and $^{16}O/^{18}O$ with galactic radius is observed (Langer & Penzias 1990; Milam et al. 2005). Such a trend arises if we assume an inside-out formation scenario for galaxies (Tang et al. 2019). If M 51 exhibits similar carbon and oxygen isotope trends, also the observed $^{13}CO/^{12}CO$ and $C^{18}O/^{12}CO$ variation can be explained.

Finally, variations in the optical depth or changes in physical conditions (e.g. gas temperature or density) of the CO isotopologues will also cause variations in the observed line ratios. For example, in LTE, the ^{12}CO optical depth depends on the gas column density, N_c, the gas velocity dispersion, σ, and the gas kinetic temperature, T_k, via $\tau \propto N_c/(\sigma T_k)$ (Paglione et al. 2001). Increased turbulence in the centre, for example, could decrease the optical depth of $^{12}CO\,(1-0)$. The trends we observe in the CO isotopologue line ratios are all consistent with changes in the optical depth.

Given the trends we find in the $^{13}CO/C^{18}O$ and $^{13}CO/^{12}CO$ line ratios, we reach a similar conclusion to Cormier et al. (2018): Abundance variations due to nucleosynthesis (assuming similar isotope trends as in the Milky Way) and/or changes in the physical conditions (temperature, density, opacity) of the gas can explain the global observed CO isotopologue line ratio variations. We recognise that most likely we are seeing a combination of effect that depends further on the SF history and chemical enrichment.

5.5. CO spectral line energy distribution

In the previous sections, we have discussed variations we find in the CO line ratios. Here, we want to further analyse in particular ^{12}CO excitation, which is relevant, for example, to accurately estimate molecular gas masses at high redshift where CO low-J transitions are difficult to obtain. Converting CO luminosities to H_2 gas masses generally relies on observations of the $^{12}CO\,(1-0)$ transition, or via down-conversion of observed higher-J observations. In particular high redshift studies rely on such down-conversions (Solomon & Vanden Bout 2005; Carilli & Walter 2013). A proper down-conversion requires a good understanding of the CO SLED. Using the three rotational transitions of ^{12}CO presented in this study, $J = 1 \rightarrow 0$, $2 \rightarrow 1$ and $3 \rightarrow 2$, we can investigate the CO SLED. As described by Narayanan & Krumholz (2014), the CO excitation, and thus the precise shape of the SLED, is expected to depend on gas temperatures, densities, and optical depth within the ISM. Consequently, we do not expect that the CO SLED is constant across the galaxy. In their study, Narayanan & Krumholz (2014) provided a parametrisation of the CO SLED as a function of SFR surface density. In Fig. 16, we investigate variations in the CO SLED with galactocentric radius, galactic morphology and SFR surface density. We see that, with the exception of sight lines within the central 1 kpc radius (which are also impacted by the central active galactic nucleus), the CO SLED has reached its turning point already at $J = 2 \rightarrow 1$. The shapes of the CO SLEDs for arm and interarm regions are very similar. But we see that variations in the CO SLED as a function of Σ_{SFR} do not follow the model presented in Narayanan & Krumholz (2014), as in particular the $^{12}CO\,(3-2)$ line seems to be fainter than the predictions of the models (see right panel in Fig. 16). In their study, they compared their model mainly to high-z sub-millimetre galaxies (SMGs). As SMGs exhibit more extreme star formation, the ISM conditions are very likely different in terms of gas temperature and density from the conditions present in M 51, which could explain the discrepancy of the CO SLED in M 51 and predicted by the models.

We note that there are also other explanations for a depression of the CO SLED relative to the models. If the beam filling factor differs significantly between the three ^{12}CO transitions, with the beam filling factor for $^{12}CO\,(3-2)$ being the smallest, beam dilution could drive down the CO SLED. The model presented in Narayanan & Krumholz (2014) takes into account different beam filling factors for the different CO transitions. In the case of the three ^{12}CO transitions we analyse, the effect is a decrease of order 10% if we apply the model that accounts for beam filling factors. Only for higher-J transitions, the effect will increase as their emission is coming from more compact regions due to the larger excitation. For confirmation that the assumed differences in beam filling factors of the model are appropriate in the case of M 51, we would need higher resolution observations for all the three low-J transitions. Narayanan & Krumholz (2014) described other effects that may lead to discrepancy between model and observation. In particular, dust extinction, which affects the very high-J transitions more, can explain the depression of the CO SLED relative to the prediction from the model. However, as our CO lines are observed in the millimetre regime, dust effects will be minimal in a normal star-forming disc galaxy such as M 51. Consequently, we do not believe that the divergence of the observations from the model can be attributed to the effects of dust.

5.6. Molecular lines and systematic density variation

In our discussion so far, we have only focused on the CO isotopologue lines. However, molecular line ratios that include denser gas tracers (such as HCN, HNC, or HCO^+) can also be used to study the underlying molecular gas density. The picture is complex: Our working resolution of >15 arcsec/600 pc is substantially larger than the dense star-forming cores, which have sizes of 0.1−1 pc (e.g. Lada & Lada 2003; André et al. 2014). Consequently, within our beam, a large range of gas volume densities are included. Therefore, the sub-beam density distribution

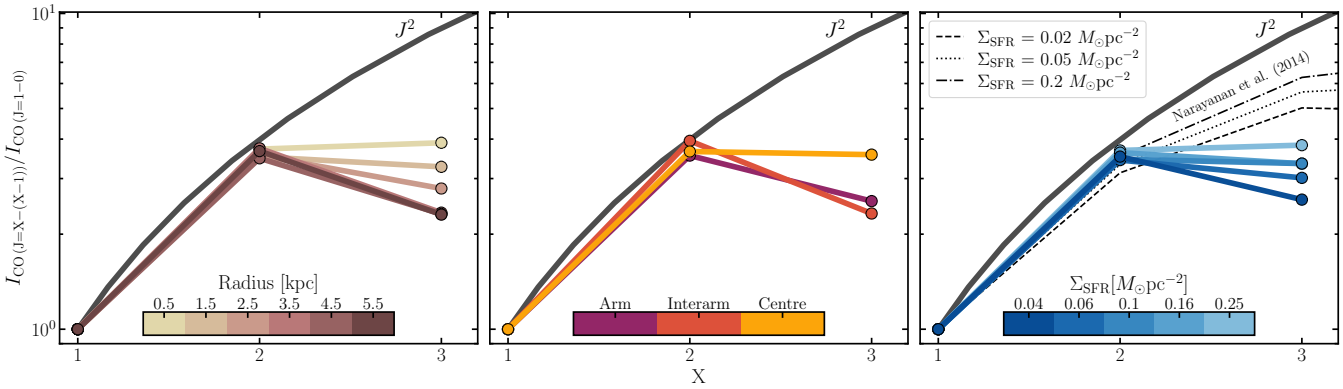

Fig. 16. CO SLED variation in M 51. *Left*: CO SLED binned by 1 kpc radial bins ranging up to 6 kpc. With the exception of the most central 1 kpc bin, we see that the CO SLED peak is already reached for $J = 2 \rightarrow 1$. *Middle*: Variation with galactic environment. The spiral arm and interarm regions show a similar CO SLED shape. *Right*: Variation as a function of SFR surface density. We include predictions for $\Sigma_{SFR} = 0.2, 0.05$, and $0.02\,M_\odot\,pc^{-2}$ based on the model code provided in Narayanan & Krumholz (2014). We use their unresolved model, which takes different beam filling factors into account for the three CO transitions. For this analysis, we use the data at a 27 arcsec working resolution.

affects the overall emission averaged over the full beam size, because certain lines emit more efficiently for a particular density distribution. Generally speaking, emission lines originate not just at or above the critical density, but the wide density distribution within our coarse observations has to be taken into account.

Leroy et al. (2017) showed by applying non-LTE radiative transfer models on a range of underlying density distributions that the line ratios of high-to-low critical density lines (i.e. emission lines with higher critical density[13]) are more sensitive to changes in gas density. For such lines, a substantial fraction of the emission can originate from regions that have a density below the nominal critical density. They based their predictions on basic radiative transfer models and a parametrised density probability distribution to characterise the effect of sub-beam density variations on the observed beam-averaged emission. The crucial point is that a line can still be emitted at densities much below the critical density, just with a reduced emissivity. Consequently, a slight increase in the gas density can significantly increase the emissivity of the emission line. This is not the case for lines with low critical density. The gas density generally exceeds the critical density already for such lines, so a variation in the gas density will not significantly impact the emissivity of the emission line.

The lines observed as part of our sample as well as the ancillary lines can be used to test whether lines with higher critical density show a larger scatter in the line ratio with respect to CO (1–0). We stack the data by CO (1–0) brightness temperature and compute the line ratio with respect to CO (1–0). In Fig. 17, we normalise the line ratios by the median value for each line ratio. Lines with a higher critical density are shown towards the right end of the plot. We colour-code the points by binned CO (1–0) brightness temperature, which we use as a shorthand for gas density. There is a distinct increase in the variation (a 'flaring') in the line ratio pattern towards higher-density tracers, in agreement with the predictions from Leroy et al. (2017), as these lines are more sensitive to variations in the sub-beam gas density distribution. This is already apparent from looking at the ^{12}CO transitions. The critical density of

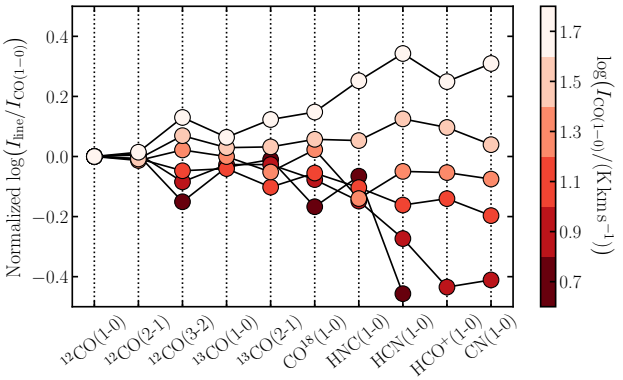

Fig. 17. Patterns of molecular line ratios for M 51. Each molecular line is stacked by CO (1–0), and the line ratio is normalised by the mean stacked line ratio with CO (1–0). We colour-coded by the CO (1–0) line brightness of the stacked bin. The line ratios are roughly ordered from left to right by increasing critical density of the line entering in the numerator. We find an increase in the line ratio variations towards the right end of the plot. Such a trend is in agreement with the results from the models presented in Leroy et al. (2017).

^{12}CO (3–2) is about an order of magnitude larger than for the (2–1) and (1–0) transitions (in the optically thin case; Carilli & Walter 2013) and we clearly find a larger variation in the ratio with ^{12}CO (3–2)/(1–0) than in the ^{12}CO (2–1)/(1–0) line ratio.

With this analysis, we thus find a larger dynamical range of line ratios of lines with a large difference in critical density. This supports the idea that the flaring pattern seen in Fig. 17 is in agreement with the higher sensitivity of these line ratios with respect to the mean gas density. Line ratio patterns of such a diverse suite of lines are thus a powerful tool for constraining the molecular gas physical conditions.

6. Conclusion

In this paper, we present observations of several CO isotopologues in the galaxy M 51 obtained with the IRAM 30 m telescope. Besides $J = 1 \rightarrow 0$ and $J = 2 \rightarrow 1$ transitions of ^{13}CO and C^{18}O, we also detect C^{17}O (1–0) emission as well as supplementary lines, such as CN (1–0), CS (2–1), N_2H^+ (1–0), and CH_3OH (2–1):

[13] For our qualitative discussion in this section, we do not go into detail regarding the various definitions of critical densities. See Leroy et al. (2017) or Shirley (2015) for a more in-depth discussion of the various definitions and their advantage and disadvantages in describing the conditions of efficient line emission.

1. We study the CO isotopologue line ratios as a function of galactocentric radius, ^{12}CO (2−1) intensities (which translates to molecular mass surface density), and TIR surface brightness (which is correlated with the SFR surface density). Several line ratios, such as ^{12}CO (2−1)/(1−0), ^{12}CO (3−2)/(2−1), and ^{13}CO (2−1)/(1−0), show a significant increase of order 5 to 40% towards the centre of the galaxy compared to their disc-averaged line ratios;
2. Galactic morphology, such as spiral arm and interarm regions, seems to affect several line ratios. In addition to increased line ratios in the centre, ^{12}CO (2−1)/(1−0) and ^{13}CO/^{12}CO(1−0) show indications of larger values in interarm regions than in spiral arm regions. Previous studies attributed an increase in the ^{12}CO (2−1)/(1−0) line ratio to the more efficient dust heating by bright, young stars (<100 Myr) at the convex, downstream end of the spiral arm. We do not, however, see any trend in the line ratio with either UV or infrared radiation;
3. We investigate the potential cause for the observed variations in the ^{13}CO/^{12}CO, C^{18}O/^{12}CO, and C^{18}O/^{13}CO line ratios. A change in optical depth most likely explains the trend seen with galactocentric radius and TIR surface density, which indicates that abundance variations in the CO isotopologues are not the cause;
4. The shape of the CO spectral energy distribution varies with galactic environment. We find a relation between the shape of the CO SLED and the SFR surface density, but the turning point of the CO SLED shape is at a lower J than predicted by recent models, which are mostly calibrated on high-z SMGs.

As a potential future study, high-quality observations at low spatial resolutions can be combined with higher spatially resolved observations to also study the diffuse CO component for the CO isotopologues and furthermore investigate line ratio variation at different spatial scales. In addition, by performing non-LTE analyses using modelling tools, it can be possible to gain further constraints on the CO-to-H_2 conversion factor or – in combination with dense gas data from EMPIRE (HCN, HCO$^+$, and HNC (1–0)) – the probability density function. This will improve constraints on the average volume density, which constituted one of the major science goals of the EMPIRE survey.

Acknowledgements. J.dB., F.B., J.P., A.T.B. and I.B. acknowledge funding from the European Research Council (ERC) under the European Union's Horizon 2020 research and innovation programme (grant agreement no.726384/Empire). T.S., E.S., H.A.P. and T.G.W. acknowledge funding from the European Research Council (ERC) under the European Union's Horizon 2020 research and innovation programme (grant agreement no. 694343). H.A.P. further acknowledges the Ministry of Science and Technology (MOST) of Taiwan under grant 110-2112-M-032-020-MY3. The work of AKL is partially supported by the National Science Foundation under Grants No. 1615105, 1615109 and 1653300. A.U. acknowledges support from the Spanish grants PGC2018-094671-B-I00, funded by MCIN/AEI/10.13039/501100011033 and by "ERDF A way of making Europe", and PID2019-108765GB-I00, funded by MCIN/AEI/10.13039/501100011033. E.R. acknowledges the support of the Natural Sciences and Engineering Research Council of Canada (NSERC), funding reference number RGPIN-2017-03987. C.E. acknowledges funding from the Deutsche Forschungsgemeinschaft (DFG) Sachbeihilfe, grant number BI1546/3-1. SCOG and RSK acknowledge support from the DFG via SFB 881 "The Milky Way System" (sub-projects B1, B2 and B8) and from the Heidelberg cluster of excellence EXC 2181-390900948 "STRUCTURES: a unifying approach to emergent phenomena in the physical world, mathematics, and complex data", funded by the German Excellence Strategy. R.S.K. furthermore thanks for financial support from the European Research Council via the Synergy Grant "ECOGAL" (grant 855130). J.M.D.K. gratefully acknowledges funding from the Deutsche Forschungsgemeinschaft (DFG, German Research Foundation) through an Emmy Noether Research Group (grant number KR4801/1-1) and the DFG Sachbeihilfe (grant number KR4801/2-1), as well as from the European Research Council (ERC) under the European Union's Horizon 2020 research and innovation programme via the ERC Starting Grant MUSTANG (grant agreement number 714907). For our research, we made use of Astropy and affiliated packages. Astropy is a community-developed core Python package for Astronomy (Astropy Collaboration 2018). Furthermore, we employed the Python package NumPy (Harris et al. 2020), SciPy (Virtanen et al. 2020), and APLpy, an open-source plotting package for Python (Robitaille & Bressert 2012).

References

Accurso, G., Saintonge, A., Catinella, B., et al. 2017, MNRAS, 470, 4750
Aladro, R., Viti, S., Bayet, E., et al. 2013, A&A, 549, A39
André, P., Di Francesco, J., Ward-Thompson, D., et al. 2014, in Protostars and Planets VI, eds. H. Beuther, R. S. Klessen, C. P. Dullemond, & T. Henning, 27
Aniano, G., Draine, B. T., Gordon, K. D., & Sandstrom, K. 2011, PASP, 123, 1218
Astropy Collaboration (Price-Whelan, A. M., et al.) 2018, AJ, 156, 123
Bensch, F., Panis, J. F., Stutzki, J., Heithausen, A., & Falgarone, E. 1997, in Astronomische Gesellschaft Abstract Series, 13, 205
Bigiel, F., Leroy, A. K., Walter, F., et al. 2011, ApJ, 730, L13
Bisbas, T. G., Tan, J. C., & Tanaka, K. E. I. 2021, MNRAS, 502, 2701
Bolatto, A. D., Wolfire, M., & Leroy, A. K. 2013, ARA&A, 51, 207
Brown, T., & Wilson, C. D. 2019, ApJ, 879, 17
Cañameras, R., Yang, C., Nesvadba, N. P. H., et al. 2018, A&A, 620, A61
Cao, Y., Wong, T., Xue, R., et al. 2017, ApJ, 847, 33
Carilli, C. L., & Walter, F. 2013, ARA&A, 51, 105
Chevance, M., Madden, S. C., Fischer, C., et al. 2020, MNRAS, 494, 5279
Colombo, D., Meidt, S. E., Schinnerer, E., et al. 2014, ApJ, 784, 4
Cormier, D., Bigiel, F., Jiménez-Donaire, M. J., et al. 2018, MNRAS, 475, 3909
Costagliola, F., Aalto, S., Rodriguez, M. I., et al. 2011, A&A, 528, A30
Croux, C., & Dehon, C. 2010, Stat. Meth. Appl., 19, 497
Dale, D. A., Cohen, S. A., Johnson, L. C., et al. 2009, ApJ, 703, 517
Davis, T. A. 2014, MNRAS, 445, 2378
den Brok, J. S., Chatzigiannakis, D., Bigiel, F., et al. 2021, MNRAS, 504, 3221
Dullemond, C. P., Juhasz, A., Pohl, A., et al. 2012, RADMC-3D: A multi-purpose radiative transfer tool
Galametz, M., Kennicutt, R. C., Calzetti, D., et al. 2013, MNRAS, 431, 1956
Genzel, R., Tacconi, L. J., Combes, F., et al. 2012, ApJ, 746, 69
Gong, M., Ostriker, E. C., & Kim, C.-G. 2018, ApJ, 858, 16
Gong, M., Ostriker, E. C., Kim, C.-G., & Kim, J.-G. 2020, ApJ, 903, 142
Gratier, P., Braine, J., Schuster, K., et al. 2017, A&A, 600, A27
Greve, T. R., Papadopoulos, P. P., Gao, Y., & Radford, S. J. E. 2009, ApJ, 692, 1432
Harris, C. R., Millman, K. J., van der Walt, S. J., et al. 2020, Nature, 585, 357
Hasegawa, T. 1997, in IAU Symposium, ed. W. B. Latter, S. J. E. Radford, P. R. Jewell, J. G. Mangum, & J. Bally, 170, 39
Hasegawa, T., Morino, J., Sorai, K., et al. 1997, in Astronomical Society of the Pacific Conference Series, Diffuse Infrared Radiation and the IRTS, eds. H. Okuda, T. Matsumoto, & T. Rollig, 124, 244
Henkel, C., Wilson, T. L., Langer, N., Chin, Y. N., & Mauersberger, R. 1994, Interstellar CNO Isotope Ratios, (Springer), 439, 72
Henkel, C., Asiri, H., Ao, Y., et al. 2014, A&A, 565, A3
Heyer, M., & Dame, T. M. 2015, ARA&A, 53, 583
Jiménez-Donaire, M. J., Bigiel, F., Leroy, A. K., et al. 2017a, MNRAS, 466, 49
Jiménez-Donaire, M. J., Cormier, D., Bigiel, F., et al. 2017b, ApJ, 836, L29
Jiménez-Donaire, M. J., Bigiel, F., Leroy, A. K., et al. 2019, ApJ, 880, 127
Keene, J., Schilke, P., Kooi, J., et al. 1998, ApJ, 494, L107
Kennicutt, R. C., & Evans, N. J. 2012, ARA&A, 50, 531
Koda, J., Sawada, T., Wright, M. C. H., et al. 2011, ApJS, 193, 19
Koda, J., Scoville, N., Hasegawa, T., et al. 2012, ApJ, 761, 41
Koda, J., Sawada, T., Sakamoto, K., et al. 2020, ApJ, 890, L10
Kramer, C., Peñalver, J., & Greve, A. 2013, Observational examples of spectral line calibration at the 30m telescope with MRTCAL and MIRA
Lada, C. J., & Lada, E. A. 2003, ARA&A, 41, 57
Langer, W. D., & Penzias, A. A. 1990, ApJ, 357, 477
Leroy, A. K., Walter, F., Brinks, E., et al. 2008, AJ, 136, 2782
Leroy, A. K., Walter, F., Bigiel, F., et al. 2009, AJ, 137, 4670
Leroy, A. K., Bolatto, A., Gordon, K., et al. 2011a, ApJ, 737, 12
Leroy, A. K., Walter, F., Schruba, A., et al. 2011b, in American Astronomical Society Meeting Abstracts, 217, 246.14
Leroy, A. K., Walter, F., Sandstrom, K., et al. 2013, AJ, 146, 19
Leroy, A. K., Walter, F., Martini, P., et al. 2015, ApJ, 814, 83
Leroy, A. K., Usero, A., Schruba, A., et al. 2017, ApJ, 835, 217
Leroy, A. K., Sandstrom, K. M., Lang, D., et al. 2019, ApJS, 244, 24
Leroy, A. K., Rosolowsky, E., Usero, A., et al. 2022, ApJ, 927, 149
Lisenfeld, U., Espada, D., Verdes-Montenegro, L., et al. 2011, A&A, 534, A102

Lundgren, A. A., Wiklind, T., Olofsson, H., & Rydbeck, G. 2004, A&A, 413, 505
Madden, S. C., Cormier, D., Hony, S., et al. 2020, A&A, 643, A141
Marka, C., Pety, J., Bardeau, S., & Sievers, A. 2017, Improvement of the IRAM 30mTelescope Beam Pattern, Tech. Rep. 2013-1
Martín, S., Aladro, R., Martín-Pintado, J., & Mauersberger, R. 2010, A&A, 522, A62
Matsushita, S., Iono, D., Petitpas, G. R., et al. 2009, ApJ, 693, 56
McQuinn, K. B. W., Skillman, E. D., Dolphin, A. E., Berg, D., & Kennicutt, R. 2016, ApJ, 826, 21
Meier, D. S., & Turner, J. L. 2004, AJ, 127, 2069
Meier, D. S., Walter, F., Bolatto, A. D., et al. 2015, ApJ, 801, 63
Milam, S. N., Savage, C., Brewster, M. A., Ziurys, L. M., & Wyckoff, S. 2005, ApJ, 634, 1126
Moustakas, J., Kennicutt, Robert C., J., Tremonti, C. A., et al. 2010, ApJS, 190, 233
Murphy, E. J., Condon, J. J., Schinnerer, E., et al. 2011, ApJ, 737, 67
Mutchler, M., Beckwith, S. V. W., Bond, H., et al. 2005, in American Astronomical Society Meeting Abstracts, Vol. 206, 13.07
Nakai, N., & Kuno, N. 1995, PASJ, 47, 761
Narayanan, D., & Krumholz, M. R. 2014, MNRAS, 442, 1411
Paglione, T. A. D., Wall, W. F., Young, J. S., et al. 2001, ApJS, 135, 183
Parkin, T. J., Wilson, C. D., Schirm, M. R. P., et al. 2013, ApJ, 776, 65
Peñaloza, C. H., Clark, P. C., Glover, S. C. O., Shetty, R., & Klessen, R. S. 2017, MNRAS, 465, 2277
Peñaloza, C. H., Clark, P. C., Glover, S. C. O., & Klessen, R. S. 2018, MNRAS, 475, 1508
Pety, J., Schinnerer, E., Leroy, A. K., et al. 2013, ApJ, 779, 43
Pineda, J. E., Caselli, P., & Goodman, A. A. 2008, ApJ, 679, 481
Pineda, J. L., Stutzki, J., Buchbender, C., et al. 2020, ApJ, 900, 132
Prantzos, N., Aubert, O., & Audouze, J. 1996, A&A, 309, 760
Puschnig, J., Hayes, M., Östlin, G., et al. 2020, A&A, 644, A10
Querejeta, M., Schinnerer, E., García-Burillo, S., et al. 2016, A&A, 593, A118
Querejeta, M., Schinnerer, E., Schruba, A., et al. 2019, A&A, 625, A19
Robitaille, T., & Bressert, E. 2012, APLpy: Astronomical Plotting Library in Python
Sage, L. J., Mauersberger, R., & Henkel, C. 1991, A&A, 249, 31
Sakamoto, S., Hasegawa, T., Handa, T., Hayashi, M., & Oka, T. 1997, ApJ, 486, 276
Sandstrom, K. M., Leroy, A. K., Walter, F., et al. 2013, ApJ, 777, 5
Sawada, T., Hasegawa, T., Handa, T., et al. 2001, ApJS, 136, 189
Schinnerer, E., Weiß, A., Aalto, S., & Scoville, N. Z. 2010, ApJ, 719, 1588
Schinnerer, E., Meidt, S. E., Pety, J., et al. 2013, ApJ, 779, 42
Schruba, A., Leroy, A. K., Walter, F., et al. 2012, AJ, 143, 138
Schuster, K. F., Kramer, C., Hitschfeld, M., Garcia-Burillo, S., & Mookerjea, B. 2007, A&A, 461, 143
Shetty, R., Vogel, S. N., Ostriker, E. C., & Teuben, P. J. 2007, ApJ, 665, 1138
Shetty, R., Glover, S. C., Dullemond, C. P., & Klessen, R. S. 2011a, MNRAS, 412, 1686
Shetty, R., Glover, S. C., Dullemond, C. P., et al. 2011b, MNRAS, 415, 3253
Shirley, Y. L. 2015, PASP, 127, 299
Sliwa, K., & Downes, D. 2017, A&A, 604, A2
Sliwa, K., Wilson, C. D., Aalto, S., & Privon, G. C. 2017, ApJ, 840, L11
Solomon, P. M., Rivolo, A. R., Barrett, J., & Yahil, A. 1987, ApJ, 319, 730
Solomon, P. M., & Vanden Bout, P. A. 2005, ARA&A, 43, 677
Sun, J., Leroy, A. K., Schinnerer, E., et al. 2020, ApJ, 901, L8
Tacconi, L. J., Genzel, R., Smail, I., et al. 2008, ApJ, 680, 246
Tan, Q.-H., Gao, Y., Zhang, Z.-Y., & Xia, X.-Y. 2011, Res. Astron. Astrophys., 11, 787
Tang, X. D., Henkel, C., Menten, K. M., et al. 2019, A&A, 629, A6
Tully, R. B., Rizzi, L., Shaya, E. J., et al. 2009, AJ, 138, 323
Usero, A., Leroy, A. K., Walter, F., et al. 2015, AJ, 150, 115
van Dishoeck, E. F., & Black, J. H. 1988, ApJ, 334, 771
Virtanen, P., Gommers, R., Oliphant, T. E., et al. 2020, Nat. Methods, 17, 261
Vlahakis, C., van der Werf, P., Israel, F. P., & Tilanus, R. P. J. 2013, MNRAS, 433, 1837
Walter, F., Brinks, E., de Blok, W. J. G., et al. 2008, AJ, 136, 2563
Watanabe, Y., Sakai, N., Sorai, K., & Yamamoto, S. 2014, ApJ, 788, 4
Watanabe, Y., Sakai, N., Sorai, K., Ueda, J., & Yamamoto, S. 2016, ApJ, 819, 144
Watson, W. D., Anicich, V. G., & Huntress, W. T., J. 1976, ApJ, 205, L165
Westerhout, G., Wendlandt, H. U., & Harten, R. H. 1973, AJ, 78, 569
Williams, T. G., Gear, W. K., & Smith, M. W. L. 2018, MNRAS, 479, 297
Wilson, T. L., & Matteucci, F. 1992, A&ARv, 4, 1
Wilson, T. L., & Rood, R. 1994, ARA&A, 32, 191
Wilson, T. L., Rohlfs, K., & Hüttemeister, S. 2009, Tools of Radio Astronomy (Springer)
Wilson, C. D., Warren, B. E., Israel, F. P., et al. 2012, MNRAS, 424, 3050
Wouterloot, J. G. A., Brand, J., & Henkel, C. 2005, A&A, 430, 549
Yajima, Y., Sorai, K., Miyamoto, Y., et al. 2021, PASJ, 73, 257
Yoda, T., Handa, T., Kohno, K., et al. 2010, PASJ, 62, 1277
Young, J. S., & Scoville, N. 1982, ApJ, 260, L11
Zhang, Z.-Y., Romano, D., Ivison, R. J., Papadopoulos, P. P., & Matteucci, F. 2018, Nature, 558, 260

Appendix A: IRAM 30 m error beam contribution

In this appendix we analyse the impact of the IRAM 30-m error beam on the detection of extended emission in our dataset. The response of the telescope to a point source is not a single perfect Gaussian, but has an additional contribution from the so-called error beams. Greve et al. (2009) characterised these error beams as a series of 2D Gaussians broader than the main beam but with a lesser contribution to the telescope power. The telescope beam patter was characterised again by Kramer et al. (2013) after the last major upgrade. The most recent characterisation implies that a point source of 1 Jy will only provide about 0.8 and 0.6 Jy in the telescope main beam at 3 and 1 mm, respectively, the flux remainder being scattered in the error beams. The image of a point source by the telescope will appear fainter at its actual position and the point source will contribute a faint extended brightness halo around it. This can be potentially critical when observing fainter positions inside a galaxy (e.g. interarm positions), as emission from brighter central parts of the galaxy will boost the detected line brightness. For similar observations with the IRAM 30 m telescope, Pety et al. (2013) first modelled the contributions of bright M 51 sources on the interarm signal (see their appendix C), and Leroy et al. (2015) proposed a first iterative deconvolution solution. We note that other deconvolution schemes had been proposed in the past (e.g. Westerhout et al. 1973; Bensch et al. 1997; Lundgren et al. 2004). We describe here the method we use to extract the contribution of the error beam to the emission and investigate its extent. This method will be precised in P. Tarrio et al. (in prep.). It should be noted that we perform the succeeding error beam estimation after attempt to correct for the main beam efficiency, but that this correction had assumed a signal free error beam, which may not be correct. So here we account for what happens when there is emission from the galaxy in the (assumed empty) error beam.

Appendix A.1: Model of the error beam

The exact pattern and shape of the error beam is hard to measure. It evolves as a function of the telescope's elevation because of gravitational deformation of the primary dish. It also depends on the evolution of the thermal environment, in particular at sunrise and sunset. We relied on the beam pattern characterisation by Kramer et al. (2013). This characterisation comes from on-the-fly measurements of the Moon edge at the IRAM 30 m optimal elevation of ~50 deg. Table A.1 lists the details of the error beam parameters used here.

In essence, we are interested in the underlying, ideal, error beam corrected main brightness temperature $\hat{T}_{\rm mb}$. The main brightness temperature is not to be confused with the intrinsic brightness temperature in the sky, T. They are related via

$$\hat{T}_{\rm mb} = G_0 \otimes T, \tag{A.1}$$

where we indicate the main beam, which has a shape of a 2D circular Gaussian, by G_0. Similarly, following Kramer et al. (2013), we assumed that the error beam also consists of a set of wide 2D Gaussian beams, indicated by G_i, where $i = 1, 2, 3$ (see Table A.1).

With the telescope, we only have access to the measured brightness in $T_{\rm A}^{\star}$ unit, which we initially converted to $T_{\rm mb}$ (the brightness temperature we use in the main text) under the simplifying assumption of an empty error beam:

$$\frac{F_{\rm eff}}{B_{\rm eff}} \times T_{\rm A}^{\star} = T_{\rm mb}, \tag{A.2}$$

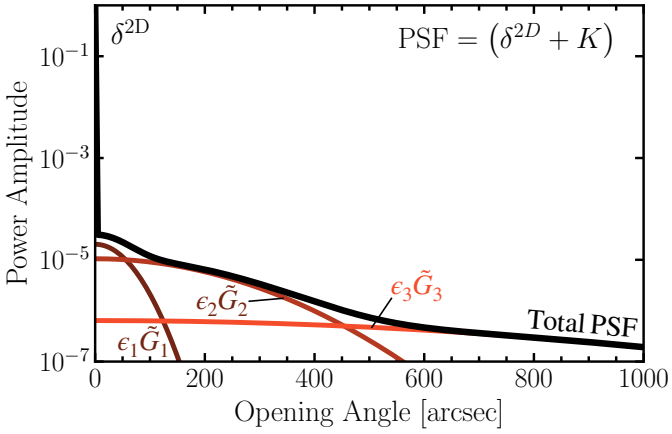

Fig. A.1. IRAM 30 m full kernel for the error beam contribution analysis after deconvolution of the main beam, G_0, for 3 mm. The kernel includes the three components of the error beam ($\tilde{G}_i$ indicates the Gaussian 2D profile after deconvolution with G_0). The ratio of the relative beam power (P_i) with respect to the relative main beam power (P_0) is indicated by $\epsilon_i = P_i/P_0$.

with the forward efficiency $F_{\rm eff}$ and the beam efficiency $B_{\rm eff}$.

The error beam corrected brightness temperature $\hat{T}_{\rm mb}$ is related to $T_{\rm mb}$ via the convolution kernel K as follows (see Figure A.1):

$$T_{\rm mb} = (\delta^{2D} + K) \otimes \hat{T}_{\rm mb}\ , \tag{A.3}$$

where δ^{2D} is the Dirac 2D distribution and the kernel K is the sum of the error beams components, after deconvolution by the main beam:

$$K = \sum_{i=1}^{3} \epsilon_i \tilde{G}_i\ , \tag{A.4}$$

where $\epsilon_i = P_i/P_0$ with P_i being the relative beam power and $\tilde{G}_i$ the deconvolution with the main beam ($G_i = \tilde{G}_i \otimes G_0$, $\tilde{\theta}_i^2 = \theta_i^2 - \theta_0^2$). Because the error beam consists of very wide 2D Gaussians, we can deconvolve the narrower main beam and get a well behaved function. Finally, to estimate the error beam contribution we have to perform a further deconvolution on Equation A.3 to determine $\hat{T}_{\rm mb}$.

Appendix A.2: Deconvolution

There are two ways in which we can approximate the error beam free source brightness temperature $\hat{T}_{\rm mb}$. The first is an iterative solution in the image plane. This approach, first described in Leroy et al. (2015), elaborates on the statement by Pety et al. (2013) that the bright intensity part of a galaxy can be approximated by the measured brightness in $T_{\rm mb}$ unit. It is possible to determine the error beam contribution by convolving the measured brightness in $T_{\rm mb}$ unit with the error beam part of the point spread function of the telescope. This gives another estimation of the source brightness that can be then used iteratively to improve the solution. In particular, we define the $N^{\rm th}$ approximate solution via the following recursion:

$$\hat{T}_{{\rm mb}|N} = T_{\rm mb} - K \otimes \hat{T}_{{\rm mb}|N-1}, \tag{A.5}$$

with $\hat{T}_{{\rm mb}|0} \equiv T_{\rm mb}$. This iterative process is stopped when the difference between two estimations becomes smaller than a give criterion.

Table A.1. Error beam parameters based on a cubic interpolation from Table 1 in Kramer et al. (2013).

	Main Beam	1. Error Beam	2. Error Beam	3. Error Beam
115.3 GHz				
Beam Width θ	21″	113″	434″	1518″
Integrated relative power P [%]	84	1	9	6
230.5 GHz				
Beam Width θ	10″	56″	217″	759″
Integrated relative power P [%]	69	5	13	13

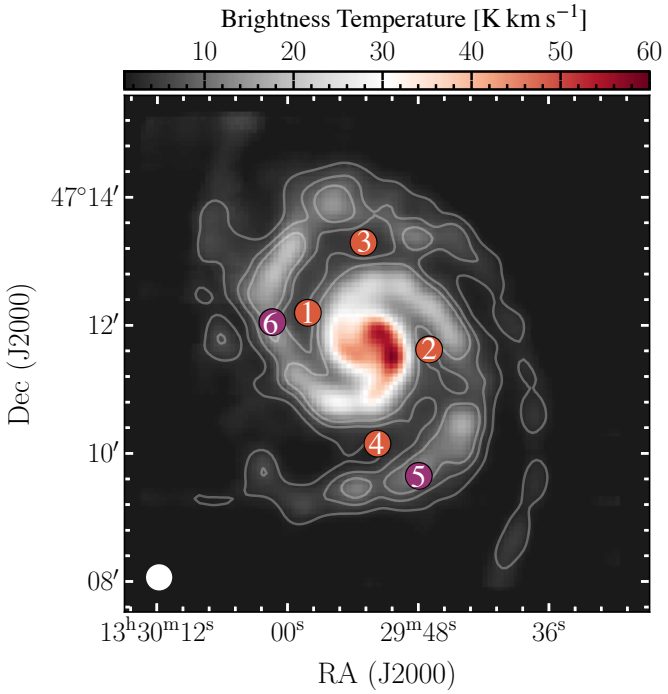

Fig. A.2. CO (2−1) line brightness temperature map. Indicated are the six pointings for which we performed the error beam correction analysis in Figure A.3. Pointings 1–4 are located in interarm regions (marked in orange). Pointings 5 and 6 are located in spiral arm regions (marked in purple). Contours are drawn at S/N = 10, 20, 30. For the IRAM 30 m DDT project E02-20, we observed these six pointings (see Appendix B.1).

The second is the Fourier plane solution. Performing a 2D Fourier transform, it follows from Equation A.3 that

$$\hat{T}_{\rm mb} = {\rm FT}^{-1}\left(\frac{{\rm FT}(T_{\rm mb})}{1+{\rm FT}(K)}\right) . \tag{A.6}$$

We implemented the approach in `Python` using the unsupervised Wiener-Hunt deconvolution (based on the Wiener-Hunt approach and estimating the hyperparameters automatically).

Appendix A.3: Result and implication

We perform the error beam contribution analysis for both the PAWS ^{12}CO (1−0) and CLAWS ^{12}CO (2−1) observations. To see the effect on the spectrum, we investigate six pointings with a 23 arcsec aperture (see Figure A.2). Four pointings (1–4) are located in the fainter interarm region and two pointings (5 and 6) are situated in the brighter spiral arm region. The result of the deconvolution can be seen in Figure A.3 for the six pointings. The blue and green spectra show $T_{\rm mb}$ (the brightness temperature we derive from $T_{\rm A}^{\star}$ assuming no error beam contributions) for ^{12}CO (1−0) and ^{12}CO (2−1) respectively. In red, we indicate the contribution to the spectrum from the error beam (i.e. $T_{\rm mb} - \hat{T}_{\rm mb}$). We indicated the percentage contribution to the $T_{\rm mb}$ integrated intensity for each pointing. This contribution is calculated only for the spectral range where S/N > 3. We performed both methods described in the Appendix A.2. Both methods yield a similar percentage contribution (< 1% point difference). We continue using the exact approach via Fourier deconvolution, since it is easier to implement. We find that for the ^{12}CO (1−0) line, the impact is minor, with the contribution ranging from ∼15 per cent in the interarm and to only 4 per cent in the spiral arm region. For the ^{12}CO (2−1) emission, because the main beam efficiency is smaller ($B_{\rm eff}^{230\,\rm GHz} \approx 60$ per cent), the contribution is more significant. In the interarm, the contribution is up to 40 per cent. This is mainly due to emission from the brighter regions in the galaxy, such as the central region, entering the observation via the different error beam components. Figure A.4 shows the full 2D map. For every pixel, we computed the error beam contribution along its spectral axis. We again see a larger effect for the ^{12}CO (2−1) emission, in particular for the interarm regions (up to 30−35 per cent).

Because the 1 mm lines are affected more than the 3 mm lines by the error beam contribution, we expect the corrected $R_{21}^{^{12}\rm CO}$ to be lower. In Table B.1, we indicate the line ratio before and after correcting for the error beam. Except for pointing 4, we still find larger $R_{21}^{^{12}\rm CO}$ values in the interarm than in the spiral arm. Consequently, even though in certain instances the error beam contribution is far from negligible, it alone cannot explain the arm/interarm trend.

We reiterate that the preceding error beam analysis is subject to many uncertainties: The exact shape of the error beam is difficult to measure and subject to temporal and positional (e.g. the elevation of the telescope) variation. Furthermore, the approach we described will generally in fact overestimate the effect of the error beam in the case of single dish maps of a galaxy. Since the error beam will be comparable to the size of the galaxy, the individual spectra will include a component consisting of a strongly convolved spectrum of the full galaxy. The baseline fitting procedure we performed will then subtract such low and broad emission in resolved observations of galaxies. So the estimated value for the error beam contribution for the different positions should be interpreted with caution. However, we believe that our measurement constitute a reasonable upper limit for the order of magnitude of the error beam contribution. We refrain from suggesting a particular constant percentage uncertainty value for general observations since the error beam contribution is not constant across the galaxy and depends strongly on the galaxy morphology. But generally, one should be aware that an additional uncertainty of order 20%-40% can be possible.

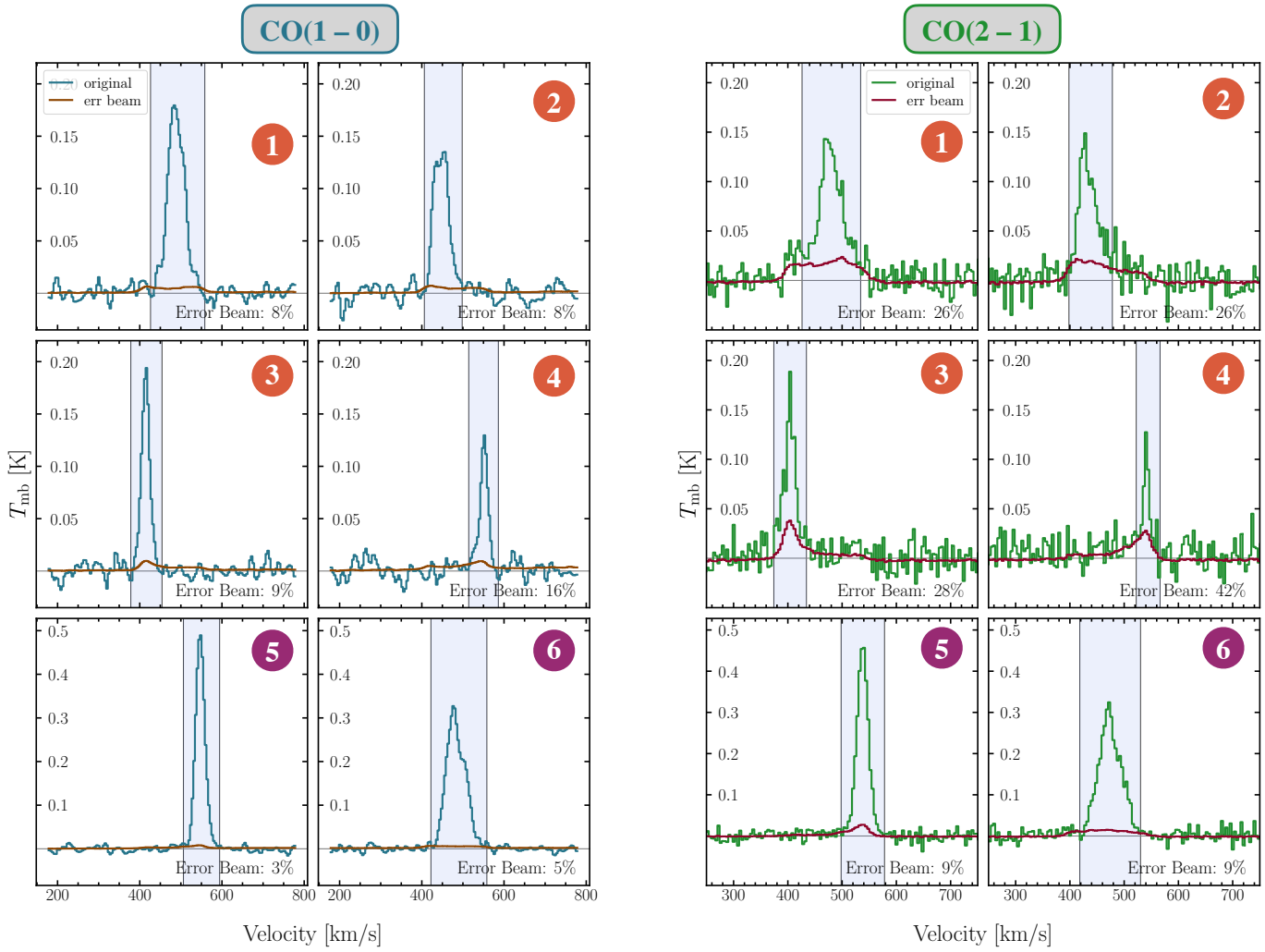

Fig. A.3. Error beam contribution analysis for individual pointings. We performed the deconvolution using the exact approach via Fourier deconvolution. After deconvolution, we performed a baseline correction. In the panels, we show the observed line brightness (T_{mb}) as well as the contribution from the error beam, $T_{mb} - \hat{T}_{mb}$. For each panel, we indicate the contribution from the error beam to the emission with S/N > 3 (see masked region). The position of the pointings is indicated in Figure A.2.

Appendix B: Flux calibration uncertainties

The flux measurements from various telescopes are subject to various degrees of calibrational uncertainties. den Brok et al. (2021) discuss in detail the impact such calibrational uncertainties can have by comparing ALMA, IRAM 30 m and NRO data. Jiménez-Donaire et al. (2019) find a flux calibration uncertainty rms of order 7 per cent for the EMIR observations from line calibrator monitoring. Finally, based on jackknifing several Heterodyne Receiver Array (HERA) datasets, Leroy et al. (2009) estimate that their HERACLES CO (2−1) observations are subject to up to a typical 20 per cent uncertainty in rms. As the data for CLAWS were observed using the EMIR instrument, which has more stable calibration than HERA, we assume our data to have an uncertainty under 10 per cent, as reported by IRAM.[14]

In this section we describe the results from the IRAM 30 m director's discretionary time (DDT) proposal, in which we observed the six pointings shown in Figure A.2 to address the flux stability in the arm and interarm to understand its impact on the arm–interarm CO line ratio.

[14] https://publicwiki.iram.es/EmirforAstronomers#Telescope_efficiencies

Appendix B.1: DDT proposal E02-20

As we have seen in the previous section, comparing datasets from different telescopes/instruments taken at different times needs extra care as uncertainties in the flux calibration can affect absolute values of line emission and ratios. den Brok et al. (2021) determined that the arm–interarm CO line ratio discrepancy contrast (and the line ratio itself) is sensitive to combining datasets from different telescopes and instruments. For example, Koda et al. (2012) find a different line ratio in the interarm region of M 51 using NRO ^{12}CO (1−0) compared to den Brok et al. (2021) and this study. Here we address the question of whether the stability of the flux calibration could explain this discrepancy.

To address this question we obtained 6 h DDT IRAM 30 m time to observe six carefully selected pointings (see Figure A.2), four in the interarm and two in the spiral arm region. As we observe CO (1−0) and ^{12}CO (2–1) simultaneously, any time dependence is removed when investigating the line ratio.

Observations were carried out on 2021 February 27 and on the night of 2021 March 8. We cannot simply take the line ratio, as the ^{12}CO (2–1) beam is smaller than the ^{12}CO (1−0) beam. To estimate how to scale the high resolution ^{12}CO (2–1) spectrum when convolving it to the resolution of ^{12}CO (1−0), we first

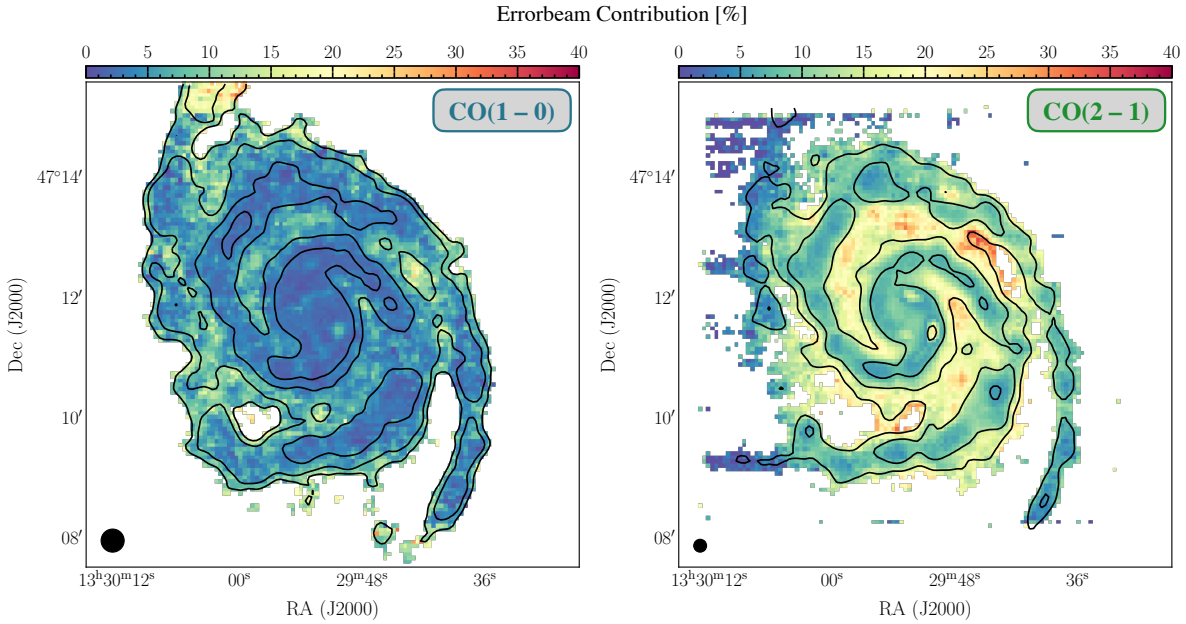

Fig. A.4. 2D distribution of the error beam contribution. (*Left*) ^{12}CO (1−0) map. Contours are drawn at S/N = 10, 20, 30 of CO (1−0) emission. (*Right*) ^{12}CO (2−1) map. We see that the error beam contribution is more pronounced for CO (2−1), in particular in the interarm regions of the galaxy.

extract a spectrum using a 11.5 arcsec (i.e. beam-sized) aperture from the CLAWS ^{12}CO (2–1) map. We then convolve the CLAWS ^{12}CO (2–1) to the lower angular resolution of 23 arcsec (i.e. PAWS resolution). We now extract a ^{12}CO (2–1) from the same position in the convolved CLAWS map, but use a 23 arcsec aperture. By comparing the two extracted ^{12}CO (2–1) spectra, we can determine a scaling factor, which we can apply to the ^{12}CO (2–1) spectrum obtained from the DDT programme.

The comparison of the line ratios is shown in Figure B.1 and the numerical values are listed in Table B.1. Circles represent the line ratio using the PAWS and CLAWS data. We notice that the line ratio is elevated in the positions of the spiral arm (1–4). Blue rectangles indicate the line ratio using the acquired DDT observations. While there is a global offset between the ratios measured in both experiments, the trend of larger line ratios in the interarm region still remains. The offset of order 20 to 30 per cent between the two datasets is mainly due to an overall calibration difference. We find that the CO (1−0) line intensities are systematically higher by 20 to 30 per cent for the DDT EMIR observations compared to the CO (1−0) data from PAWS, which reduces the line ratio overall. We note that the discrepancy between NRO and the PAWS CO (1−0) is still greater. Especially in the interarm region, the NRO data are larger by a factor of ∼2. This is related to a change of the calibration strategy of the EMIR receivers, which happened in February 2017 when the calibration software swapped from `MIRA` to `MRTCAL`. To first order, the calibration factor applied to the spectrometer data is proportional to the measured system temperature computed on the calibration scan. While `MIRA` was computing this system temperature on spectral chunks of 4 GHz, `MRTCAL` computes it every 20 MHz. Marka et al. (2017) shows that this leads to an overestimation of the system temperature for lines that lies at the edges of the atmospheric windows as this is the case for ^{12}CO (1−0) whose rest frequency lies inside the wings of the di-oxygen telluric line. In this case, calibrating the PAWS data with `MRTCAL` would lead to higher (and more accurate) system temperature, and thus higher line brightnesses.

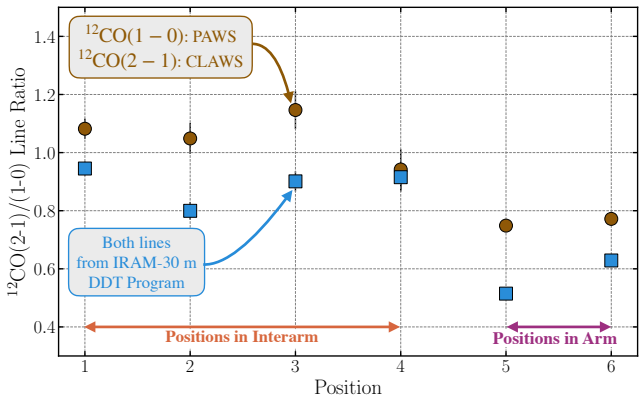

Fig. B.1. Arm–interarm CO line ratio analysis. Circles indicate the ^{12}CO (2−1)/(1−0) line ratio for lines extracted over the apertures shown in Figure A.2. The squares show the CO line ratio from the IRAM 30 m DDT project E02-20. Positions 1–4 are within the interarm of the galaxy, and positions 5 and 6 are in the spiral arm region. We see that both show larger line ratios in the interarm regions, leading us to conclude that the trend we find is not due to issues with the flux calibration uncertainties. The numerical values of the individual points are listed in Table B.1.

Relative flux calibration can be significant. But our analysis leads us to conclude that relative flux calibration is not the main cause of the arm–interarm trend, since we find also larger line ratio values in the interarm region using the newer IRAM 30 m DDT observations.

Appendix C: Products for public data release

Along with this survey paper, we provide several data products for the various spectral lines. The data products are stored on

Table B.1. Comparison of the ^{12}CO (2–1)/(1–0) line ratio within the selected positions, 1–6, using either the CLAWS ^{12}CO (2−1) and PAWS ^{12}CO (1−0) dataset or the newly acquired IRAM 30 m data from project E02-20.

	Position	$R_{21}^{^{12}CO}$		
		CLAWS/PAWS data		E02-20 data
		raw	e.b. corrected	
Interarm	1	1.08 ± 0.03	0.94 ± 0.03	0.87 ± 0.02
	2	1.05 ± 0.05	0.84 ± 0.05	0.80 ± 0.03
	3	1.15 ± 0.07	0.91 ± 0.06	0.90 ± 0.04
	4	0.94 ± 0.07	0.65 ± 0.05	0.92 ± 0.05
Arm	5	0.75 ± 0.01	0.70 ± 0.01	0.52 ± 0.01
	6	0.77 ± 0.02	0.74 ± 0.01	0.63 ± 0.01

Notes. For the CLAWS/PAWS $R_{21}^{^{12}CO}$, we provide the value without (raw) and with error beam correction (based on the error beam contribution indicated in Figure A.3).

the IRAM server.[15] The data have been processed following the methodology adopted for the IRAM Large Programmes EMPIRE (Jiménez-Donaire et al. 2019) and HERACLES (Leroy et al. 2009). The IRAM repository for Large Programmes provides the following, non-error beam corrected data products: (i) for all lines: the 3D data cubes, the rms and uncertainty maps, and the integrated brightness temperature (moment-0) maps; and (ii) for ^{12}CO (2−1) and ^{13}CO (1−0) only: the intensity-weighted velocity (moment-1) maps, the equivalent width maps, and the peak temperature maps.

We refer the reader to the `Readme` file at the IRAM data repository for more detailed information. We ask that when using this dataset or parts of it, this paper be cited.

[15] https://www.iram-institute.org/EN/content-page-434-7-158-240-434-0.html